Applied Catalysis B: Environmental 343 (2024) 123490

Contents lists available at ScienceDirect

Applied Catalysis B: Environmental

journal homepage: www.elsevier.com/locate/apcatb

Electron transfer-mediated enhancement of superoxide radical generation in fenton-like process: Key role of oxygen vacancy-regulated local electron density of cobalt sites

Ta Cong Khiem [a], Nguyen Nhat Huy [b,c], Eilhann Kwon [d], Jechan Lee [e], Wen Da Oh [f], Xiaoguang Duan [g], Stanisław Wacławek [h], Haitao Wang [i], Grzegorz Lisak [j,k], Farshid Ghanbari [l,*], Kun-Yi Andrew Lin [a,m,**]

[a] Department of Environmental Engineering & Innovation and Development Center of Sustainable Agriculture, National Chung Hsing University, Taichung 402, Taiwan
[b] Faculty of Environment and Natural Resources, Ho Chi Minh City University of Technology (HCMUT), Ho Chi Minh City 700000, Viet Nam
[c] Vietnam National University Ho Chi Minh City, Ho Chi Minh City 700000, Viet Nam
[d] Department of Earth Resources and Environmental Engineering, Hanyang University, Seong Dong-Gu, Seoul, South Korea
[e] Department of Global Smart City & School of Civil, Architectural Engineering, and Landscape Architecture, Sungkyunkwan University, Suwon 16419, Republic of Korea
[f] School of Chemical Sciences, Universiti Sains Malaysia, 11800 Penang, Malaysia
[g] School of Chemical Engineering and Advanced Materials, The University of Adelaide, SA 5005, Australia
[h] Institute for Nanomaterials, Advanced Technologies and Innovation, Technical University of Liberec, Studentská 1402/2, 461 17 Liberec 1, Czech Republic
[i] Key Laboratory o f Pollution Processes and Environmental Criteria, College of Environmental Science and Engineering, Nankai University, Tianjin 300071, China
[j] School of Civil and Environmental Engineering, Nanyang Technological University, 50 Nanyang Avenue, 639798, Singapore
[k] Residues and Resource Reclamation Centre (R3C), Nanyang Environment and Water Research Institute, Nanyang Technological University, Singapore
[l] Research Center for Environmental Contaminants (RCEC), Abadan University of Medical Sciences, Abadan, Iran
[m] Institute of Analytical and Environmental Sciences, National Tsing Hua University, Hsinchu, Taiwan

ARTICLE INFO

Keywords:
H_2O_2 activation
Fenton-like process
Electron transfer
Superoxide radical
Oxygen vacancy

ABSTRACT

Designing metal oxides with oxygen vacancy (OV) is a prospective strategy for boosted Fenton-like process. However, what OV is, whether OV enhancement increases the catalytic performance, OV-related H_2O_2 activation, and relationship between OV and ROS or non-radical pathways have not been fully understood. Herein, yolk-shell Co_3O_4 nanospheres with various OV were fabricated to overcome the above contentious problems and establish a relationship between OV, ROS, and electron transfer in sulfadiazine (SDZ) degradation via H_2O_2 activation. The results showed that the delocalized electron-rich Co sites around OV with increasing OV allowed the improved conductivity, thereby leading to stronger adsorption and activation of H_2O_2 to generate more $^{\bullet}OH$ as evidenced by the attenuated adsorption energy and prolonged O-O bond. The subsequent rapid depletion of $^{\bullet}OH$ coupled with the increase in $O_2^{\bullet-}$ over time and the emergence of electron transfer from SDZ explored a pathway enhancing $O_2^{\bullet-}$ generation for SDZ degradation.

1. Introduction

Advanced oxidation process (AOP) with hydrogen peroxide (H_2O_2)-based heterogeneous catalysis is a promising strategy, which can overcome drawbacks of Fenton processes to degrade antibiotics on account of generated reactive oxygen species (ROS) [1]. For the purpose of promoting H_2O_2 activation into ROS, many techniques have been developed so far [2–6]. In comparison with energy- and noble metal-based activation techniques, ones that use common transition metals are more affordable [7]. Utilizing defective metal oxides that combine the availability of several metal species and improved electronic characteristics induced by defects is deemed as one of the most prospective catalytic aspects [8]. Common metal oxides, such as MnO_2 [9], Fe_3O_4 [10], Co_3O_4 [11], NiO [12], Cu_2O [13], and ZnO [14], have

* Corresponding author.
** Corresponding author at: Department of Environmental Engineering & Innovation and Development Center of Sustainable Agriculture, National Chung Hsing University, Taichung 402, Taiwan.
E-mail addresses: ghanbari.env@gmail.com (F. Ghanbari), linky@nchu.edu.tw (K.-Y.A. Lin).

https://doi.org/10.1016/j.apcatb.2023.123490
Received 9 August 2023; Received in revised form 26 October 2023; Accepted 6 November 2023
Available online 10 November 2023
0926-3373/© 2023 Elsevier B.V. All rights reserved.

received a lot of study attention recently. Defects in these metal oxides could be categorized into two types, including cation (metal defect) and anion (oxygen defect or oxygen vacancy, OV). Take Co_3O_4 as an example, Li et al. have recently fabricated $Co_{3-x}O_{4-x}$ with the existence of both Co defect and OV by calcination in the air at 300 °C for 1 h followed by reduction with H_2 for 1 h at 200 °C. The resultant $Co_{3-x}O_{4-x}$ exhibited superior toluene oxidation performance in 10 min with over 90% conversion under light illumination [15]. Among the above two types of defects, OV is more common and has received the main focus in recent studies. Ding et al.'s work is a good example of this. HS-$CuFe_2O_{4-\delta}$ with OV could achieve complete degradation of ciprofloxacin (CIP) within 30 min via H_2O_2 activation with the 1st order rate constant of 0.0994 min^{-1}, 20 times higher than that of $CuFe_2O_4$, due to the presence of OV [8]. In another work by Yang et al., $M_{10}CuO$ with the most abundant OV outperformed its counterparts with lower OV (M_5CuO and $M_{15}CuO$) induced by Mn^{2+} doping in activating H_2O_2 to degrade CIP [16].

However, the underlying mechanisms behind OV-enhanced H_2O_2 activation by metal oxides are still nebulous, and four aspects are contentious: what OV is, why OV enhances the catalytic performance, how H_2O_2 is activated, and how about the relationship between OV and ROS or non-radical pathways. Firstly, what OV is has not been cleared up yet. While some researchers contend that OV is an active center with electron-rich property [16], others think that it is an electron donor [14] or an oxidant that can be activated into active oxygen species [17,18]. In fact, OV is a state in which one or more oxygen atoms are absent. Thus, such a state cannot serve as an active center, an electron donor, or an oxidant but rather adjacent metal atoms that are in unsaturated states with low valences [19].

Secondly, it remains unclear that why can OV enhance the catalytic performance? Some researchers suggest that OV has abundant localized electrons capable of accelerating the adsorption and activation behavior of H_2O_2 by prolonging O-O bond to generate more $^{\bullet}OH$ [20,21], or of peroxydisulfate [22] and small molecules [23], but one question is whether it is certain that OV possesses a lot of localized electrons while it is a state that shows the absence of oxygen atom(s) rather than it being an atom. Furthermore, the evidence that it has many localized electrons needs to be elucidated because another equally curious aspect is how about the delocalized electrons. It seems that the absence of some lattice oxygen (O_{lat}) further enhances the increase in the delocalization of adjacent metal atoms due to the unsaturated bonding. On the other hand, some believe that OV can modulate the electronic structure [24, 25] and redistribute the charge density [26,27]. Nonetheless, how does OV change these properties, positively or negatively? It is more than likely that in the presence of OV, the electronic structure and charge density of catalysts are altered, but how they are altered needs to be studied further. On the one hand it is reported that the presence of OV raises the charge density around active sites [24,28], but on the other hand, Mao et al. argued that OV with high electron density is able to stabilize intermediates and lower down the energy barriers for CO_2 photoreduction [29]. In fact, electron density and charge density are two opposite properties and cannot be varied in the same direction at the same time. As the electron density increases, the charge density decreases and vice versa. In addition, the perception of the role of OV is still quite vague, typically OV in Fe^0/CeO_2 as concluded by Zhang et al. in a recent study. Accordingly, the role of OV is believed to decrease the activation energy of H_2O_2 and enhance the adsorption of tetracycline (TC) while no convincing evidence has been provided [30].

Thirdly, whether H_2O_2 is an electron donor or electron acceptor is a subject of debate. It is widely acknowledged that H_2O_2 receives one electron from catalysts and is activated to produce $^{\bullet}OH$ via Eq. (1), which is essentially equivalent to Eq. (2), but it is once claimed that H_2O_2 loses its electrons to Fe sites in either Fe_3O_4 or V_o-Fe_3O_4 [10]. It is clear that the second assertion is completely unconvincing because the unsaturated bound state of Fe sites near OV makes these sites redundant of unpaired electrons that would readily be donated to H_2O_2. What is more, H_2O_2 is thought to accept electrons from OV when adsorption takes place at this site. However, OV is the vacancy wherein there are no any O_{lat} atoms, i.e., there will not be any adsorption bonds between OV and H_2O_2 at this site. It is worth mentioning that there is not only one bond, but up to three bonds (one from an O atom of H_2O_2 to an O_{lat} atom of V_o-Fe_3O_4, and two from two O atoms of H_2O_2 to one Fe atom). Therefore, the electron donation to H_2O_2 and the strong adsorption of H_2O_2 at this site are both completely contributed by the Fe atom near OV rather than OV.

$$H_2O_2 + e^- \rightarrow {}^{\cdot}OH + OH^- \quad (1)$$

$$M^{n+} + H_2O_2 \rightarrow M^{n+1} + {}^{\cdot}OH + OH^- \quad (2)$$

Fourthly, the presence of OV is said to improve the catalytic performance [31], so is the more OV the higher the performance? This question has so far not been satisfactorily answered. Li et al. suggested that the degradation of TC was mainly due to the contribution of $^{\bullet}OH$, but $Ca_{1.0}FeO_{3-\delta}$ with the most OV activated H_2O_2 to produce lower $^{\bullet}OH$ than $Ca_{0.9}FeO_{3-\delta}$ [32]. Meanwhile, others suggest that increasing OV increases performance, but ROS is detected only for the catalyst with the highest OV [33]. This raises many questions as to whether the OV increases, the ROS generated will increase or not. Furthermore, the switching mechanism between radical and non-radical pathways as OV increases will not be fully understood. Assuming in the case that OV increases and ROS increases accordingly, will ROS be generated continuously and increase over time or will it only increase at the beginning and then gradually decrease? Many current studies focus only on the detection of ROS by electron paramagnetic resonance (EPR) at a given time but do not quantify the amount of ROS generated over time [16,34]. It is possible that one species is more at first than the other, but over time there can be a conversion between them, that is, a change in reaction mechanism. Furthermore, besides ROS, there may be other species or pathways (such as high-valent metal-oxo species [35], [36,37] and electron transfer [38]) that are also involved in pollutant degradation [39], but these are often not fully detected [32,34]. Even if detected, the relationship between them and ROS has not been thoroughly studied. It is possible that some of the ROS are generated a lot in the initial stage, but through high-valent metal-oxo species or electron transfer, another of the remaining ROS is likely to increase and the ROS that is generated a lot at the beginning will decrease over time. This stimulates curiosity and needs to be studied in depth. Additionally, in most of the studies, the adsorption of H_2O_2 on the catalyst surface is only performed and compared between the catalyst with OV and without OV [40–42]. In the case of catalysts with OV, only one oxygen atom is removed from the surface [40]. This will not completely explain the increase in OV will increase the performance through the decrease in the adsorption energy (E_{ads}) between H_2O_2 and the catalyst surface. Therefore, it is necessary to carry out the adsorption of H_2O_2 on the catalyst surface with more than one OV.

Herein, yolk-shell Co_3O_4 nanospheres with various OV (YCO-X) were prepared by using cobalt glycerate (CoG)-derived hierarchical yolk-shell α-$Co(OH)_2$ nanospheres (YCH) and reduction method with $NaBH_4$. Effects of OV on the electronic structure of YCO-X and the adsorption of H_2O_2 on YCO-X surfaces were investigated by density-functional theory (DFT) calculations, while the generation of ROS was measured through quantitative experiments. The results showed that delocalized electron-rich Co sites around OV served as active sites for the boosted H_2O_2 adsorption and $^{\bullet}OH$ generation. Based on the negligible contribution of $^{\bullet}OH$ to the degradation of sulfadiazine (SDZ) in YCO-3/H_2O_2 system and the relationship between $^{\bullet}OH$, $O_2^{\bullet-}$, and SDZ, the enhanced generation of $O_2^{\bullet-}$ mediated by the electron transfer of SDZ to H_2O_2 via YCO-3 was proven. This study not only overcame and resolved lingering questions from previous studies, but also uncovered a new pathway enhancing the $O_2^{\bullet-}$ generation in Fenton-like process.

2. Materials and methods

2.1. YCO-0 preparation

CoG prepared using the method in Text S2 was firstly transformed into YCH by reacting with urea. CoG (240 mg) was dispersed in 90 mL of ethanol (EtOH, 95%) and 30 mL of deionized (DI) water for 15 min 1200 mg urea were subsequently added to the mixture and stirred for 5 min before being heating at 100 °C for 2 h. The green powder (i.e., YCH) was collected by centrifugation, washed several times with EtOH before drying at 65 °C in an oven overnight. After that, YCH was calcined at 450 °C for 2 h (2 °C/min) in the air to obtain yolk-shell Co_3O_4 nanospheres (YCO-0).

2.2. YCO-X preparation

200 mg YCO-0 were stirred in 200 mL of DI water containing certain amount of $NaBH_4$ for 1 h at room temperature. The suspensions were then filtered, washed several times with DI water and 95% EtOH, and dried at 65 °C to obtain YCO-X with X equal to 1, 2, and 3 corresponding to 75.66, 378.3, and 1513.2 mg $NaBH_4$. CoG without reacting with urea was calcined at 450 °C for 2 h (2 °C/min) in the air to produce hollow Co_3O_4 nanospheres (HCO). Detailed characterizations and experimental procedures are presented in supporting information.

2.3. Electrochemical performance tests

Two types of electrochemical workstation were used. Cyclic voltammetry (CV) and linear sweep voltammetry (LSV) were performed with CHI 621D, while electrochemical impedance spectroscopy (EIS) was performed with PalmSens4 from 10^5 Hz to 10^{-2} Hz. Each of these two electrochemical workstations comprised of a working electrode (YCO-X-loaded glass carbon electrode, YCO-X @ GCE), an auxiliary electrode (platinum wire), and a reference electrode (Ag/AgCl). The analysis was conducted in 1 M KOH for CV and LSV, and 0.5 M Na_2SO_4 for EIS. Before use, a chamois leather dropped with alumina slurry was used to polish the GCE, which was washed with EtOH and DI water in an ultrasonic bath for 5 min, and dried at 65 °C. To prepare the YCO-X @ GCE, 16 mg of each YCO-X, 2 mg of carbon black, and 2 mg of polyvinylidene fluoride (PVDF) were dispersed in 1 mL of 1-methyl-2-pyrolidone under sonication for 1 h. 10 μL of the slurry were then coated on the GCE, followed by drying at 80 °C. For identification of electron transfer, all the above analyses were conducted in the 0.5 M Na_2SO_4 electrolyte containing H_2O_2 and/or SDZ. The potentials were converted from V vs. Ag/AgCl into V vs. RHE using the Nernst equation [43]:

$$E_{RHE} = E_{Ag/AgCl} + 0.1976 + pH \times 0.0592 \quad (3)$$

2.4. SDZ degradation experiments

The catalytic performance was evaluated by Fenton-like degradation of SDZ. The solution (100 mL) containing 5 mg/L SDZ and 90 mM H_2O_2 was stirred at 30 °C. After that, the reaction was started by adding 15 mg of each catalyst. During the reaction, 1.5 mL were collected regularly and injected through 0.22-μm PVDF filters for analysis. The SDZ concentration was measured with a Chrom Tech CT-2200 spectrophotometer at 261 nm. Effect of pH was investigated by adjusting the solution pH using HCl and NaOH. Other effects, such as YCO-3, H_2O_2, SDZ, methanol (MeOH), tert-butanol (TBA), *p*-benzoquinone (*p*-BQ), NaN_3, furfuryl alcohol (FFA), dimethyl sulfoxide (DMSO), or KI concentrations and temperature, were investigated by changing these to target values, while repeating the same procedure but adding humic acid (HA, 10 mg/L) or anions (10 mM) in case the effect of YCO-3, HA/anions, and temperature were considered. The reusability was conducted by utilizing YCO-3 after filtering the solution at the end of each reaction with 0.22-μm PVDF filters, washing, and drying at 65 °C. To compensate for the loss of YCO-3 after the reaction, 1000 mL were used instead and other conditions were kept. For regeneration, YCO-3 after four consecutive cycles was treated with $NaBH_4$ using the same procedure as that for its preparation. In addition, the EPR spectra of YCO-3 after four cycles of reuse and after regeneration were recorded to investigate the change in number of OV. The detail is in Text S3.

2.5. H_2O_2 consumption test

The general procedure was same as that for SDZ degradation, but SDZ was not added to the solution. During the reaction, 0.5 mL of the solution taken out were filtered and then 0.1 mL of the filtrate were combined with 3 mL of 0.4 M KI solution, 3 mL of 0.1 M potassium hydrogen phthalate solution, and 3 mL of DI water. The absorbance was determined with a spectrophotometer at 350 nm after diluting the solution to 100 mL with DI water and waiting for 30 min. The measurement of H_2O_2 with a spectrophotometer was based on the formation of triiodide ion (I_3^-), referred to as I_3^- method, according to reactions $H_2O_2 + 2I^- + 2H^+ \rightarrow I_2 + 2H_2O$ and $I_2 + I^- \rightleftharpoons I_3^-$, which has been reported in previous studies [44], [45]. In addition, a good linear response of the absorbance with H_2O_2 concentration (Fig. S1) indicated the accuracy of this method.

2.6. $O_2^{\bullet-}$ quantification procedure

The SDZ solution was replaced with nitro blue tetrazolium (NBT, 65 mg/L, 100 mL) solution, and other conditions (H_2O_2 concentration and temperature) were kept same as those for SDZ degradation. Repeat the same steps to start the reaction and take the solution out. After that, 0.5 mL of the filtrate were diluted to 50 mL with DI water. The absorbance of NBT was determined with the spectrophotometer at 259 nm [46]. The $O_2^{\bullet-}$ concentration was then determined from the reduction of NBT using Eq. (4):

$$\{6.5 - [(A_t/A_0) \times 6.5 \times 100]/817.64\} \times 4 \times 1000(\mu mol) \quad (4)$$

where 6.5 is the NBT mass (mg); A_0 and A_t are the absorbance of NBT solution at 0 and t min, respectively; 100 is the dilution factor (0.5–50 mL); 817.64 is NBT molar mass (g/mol); 4 is the stoichiometric factor between reaction of $O_2^{\bullet-}$ and NBT; 1000 is the conversion factor from mmol to μmol. Other procedures, such as $^{\bullet}OH$ quantification and FFA loss, are provided in Text S4.

3. Results and discussion

3.1. Characterizations

The preparation scheme of yolk-shell Co_3O_4 nanospheres with various OV (YCO-X) is illustrated in Fig. 1(a). Firstly, YCH was prepared from the reaction between the soft template CoG and urea via.

hydrothermal process. The formation of YCH was based on the reaction between Co^{2+} liberated from CoG and OH^- from the hydrolysis of urea via equation $Co^{2+} + 2OH^- \rightarrow Co(OH)_2$. Then, the YCH precursor was converted into YCO-0 by calcination in the air ($6Co(OH)_2 + O_2 \rightarrow 2Co_3O_4 + 6H_2O$). Finally, YCO-X was fabricated by the reduction with $NaBH_4$ at different amounts, through which Co cations in YCO-0 were reduced ($8Co^{n+} + NaBH_4 + 2H_2O \rightarrow 8Co^{(n-1)+} + NaBO_2 + 8H^+$ [25]) and OV was formed simultaneously due to the capturing effect of oxygen atoms by $NaBH_4$ via an electron transfer [47]. For comparison, HCO was also prepared by directly calcining CoG.

The morphologies of CoG and YCH are shown in Fig. S2, which shows that CoG was solid spheres with several tiny particles on the surface, while YCH had the form of hierarchical yolk-shell spheres. N_2 sorption and pore size distribution in Fig. S3 show that YCH had a N_2 sorption amount as well as a pore volume significantly higher than those of CoG,

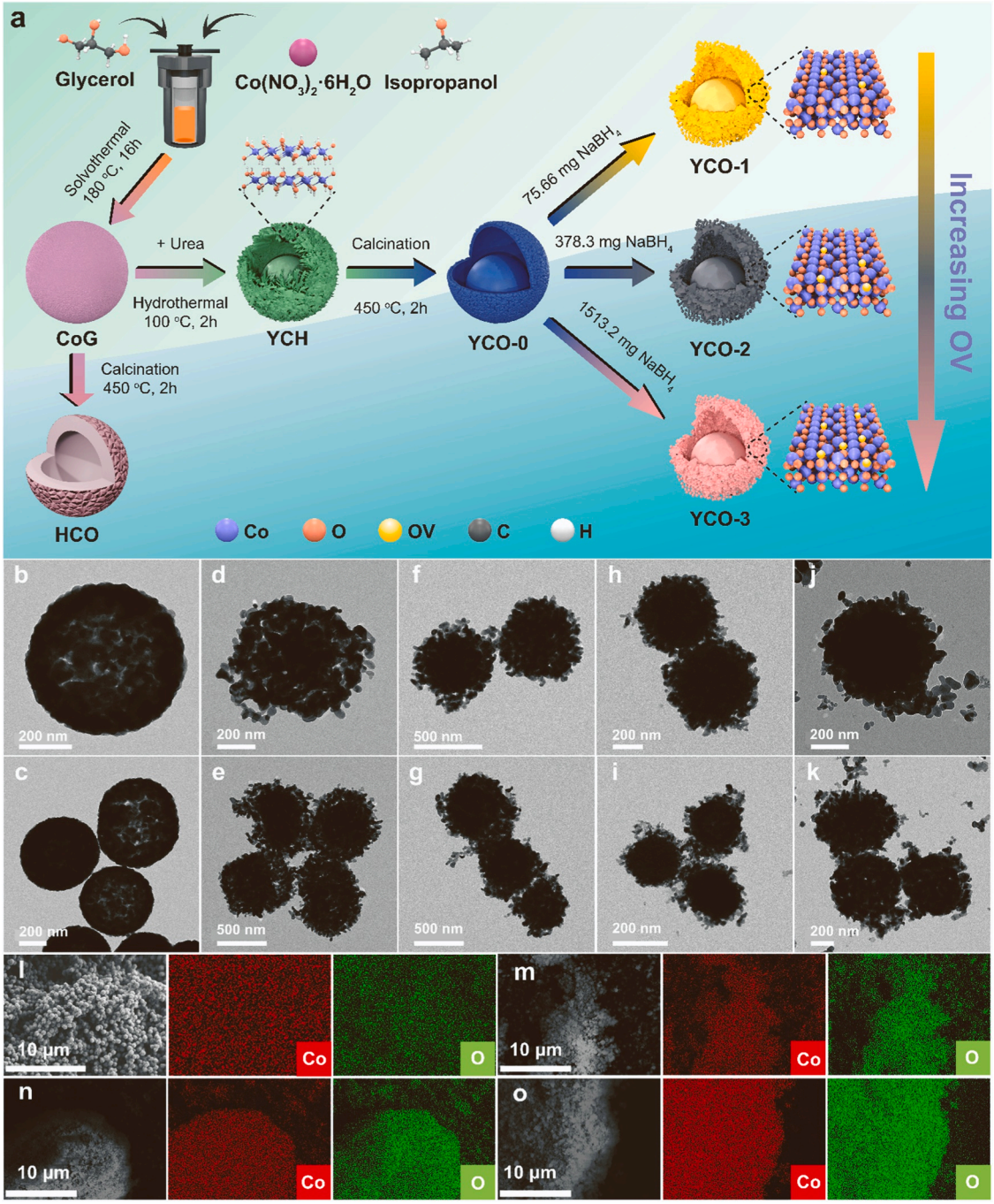

Fig. 1. (a) Preparation scheme of HCO, YCO-0, and YCO-X; (b-k) TEM images of (b, c) HCO, (d, e) YCO-0, (f, g) YCO-1, (h, i) YCO-2, and (j, k) YCO-3; and (l-o) EDS mapping images of (l) YCO-0, (m) YCO-1, (n) YCO-2, and (o) YCO-3.

Table 1
Textural and crystal properties of HCO, YCO-0, and YCO-X.

Catalyst	Surface area (m^2/g)	Pore volume (cm^3/g)	Pore diameter (nm)	d-spacing (Å)[a]	Crystallite size (nm)[a]	Lattice parameter (Å)[b]	Microstrain (%)[a]
HCO	14	0.051	1.976	2.4391	24.64	8.0752	0.4402
YCO-0	18	0.157	18.072	2.4378	23.41	8.0715	0.4636
YCO-1	24	0.161	9.785	2.4391	23.16	8.0910	0.4687
YCO-2	39	0.263	7.936	2.4404	22.00	8.0938	0.4933
YCO-3	53	0.291	1.873	2.4442	17.87	8.0829	0.6076

[a] Calculated from the (311) crystal plane using equations in Text S9.
[b] Average value obtained from (111), (220), (311), (222), (400), (422), (511), and (440) crystal planes (details in Text S9).

which made YCH a good precursor for constructing next catalysts. The internal structure of HCO, YCO-0, and YCO-X was examined by TEM images as depicted in Fig. 1(b-k). In general, HCO was nanospheres with a hollow structure. On the contrary, YCO-0 was the yolk-shell nanospheres, inherited from YCH, with a diameter of ~600 nm. After reduction, the overall yolk-shell morphology of YCO-X remained intact but several nanoparticles appeared on the surface, indicating that the surficial transformation has occurred. Thus, YCO-X are predicted to have a higher specific surface area than YCO-0. As can be seen in Fig. S4(a-e), large hysteresis loops of HCO, YCO-0, and YCO-X were observed, revealing the presence of mesopores. Among these, YCO-3 had the largest hysteresis loop with the highest peak, disclosing its highest surface area. This is confirmed by data in Table 1, in which the surface area increased gradually from 14 m^2/g of HCO to the highest value at 53 m^2/g of YCO-3, showing that the reduction can increase the surface area. Besides, the pore size distribution in Fig. S4(f-j) shows that the pore radius ranging from around 0 to below 80 nm was found in all the catalysts except YCO-3, which had the highest pore radius distribution of over 80 nm with the highest pore volume (Table 1). High surface area and pore volume are favorable for the catalytic reactions because of more active sites.

Elemental composition of the catalysts was analyzed by EDS. From Fig. S5, it is apparent that only two elements Co and O were detected, while these two elements were evenly distributed over each large selected region (Fig. 1l-o). In addition, the survey XPS spectra in Fig. S6 display only these two elements, demonstrating that these catalysts were merely Co_3O_4.

The information about crystal phases was provided by XRD patterns, and other related parameters were calculated and presented in Table 1. As shown in Fig. S7, after hydrothermal treatment, CoG was transformed into YCH with the appearance of some new peaks (8.64, 18.48, and 34.34°), which could be indexed to (003), (006), and (012) crystal planes of α-$Co(OH)_2$ (JCPDS#46–0605) [48]. Meanwhile, Fig. 2(a) shows that there were no new peaks of YCO-X appeared compared to HCO and YCO-0, demonstrating the purity of the crystal structure after reduction. However, the intensity of the diffraction peaks characteristic of (111), (220), (311), (222), (400), (422), (511), and (440) crystal planes of HCO and YCO-0 based on JCPDS#42–1467 decreased from YCO-1 to YCO-3. The decrease in the peak intensity (i.e., lower crystallinity) unveils that these YCO-X samples had a larger lattice distortion [49], resulting in the fall in the crystallite size. Thus, more lattice defects could be produced. In addition, the 2θ at 36.94° characteristic of the

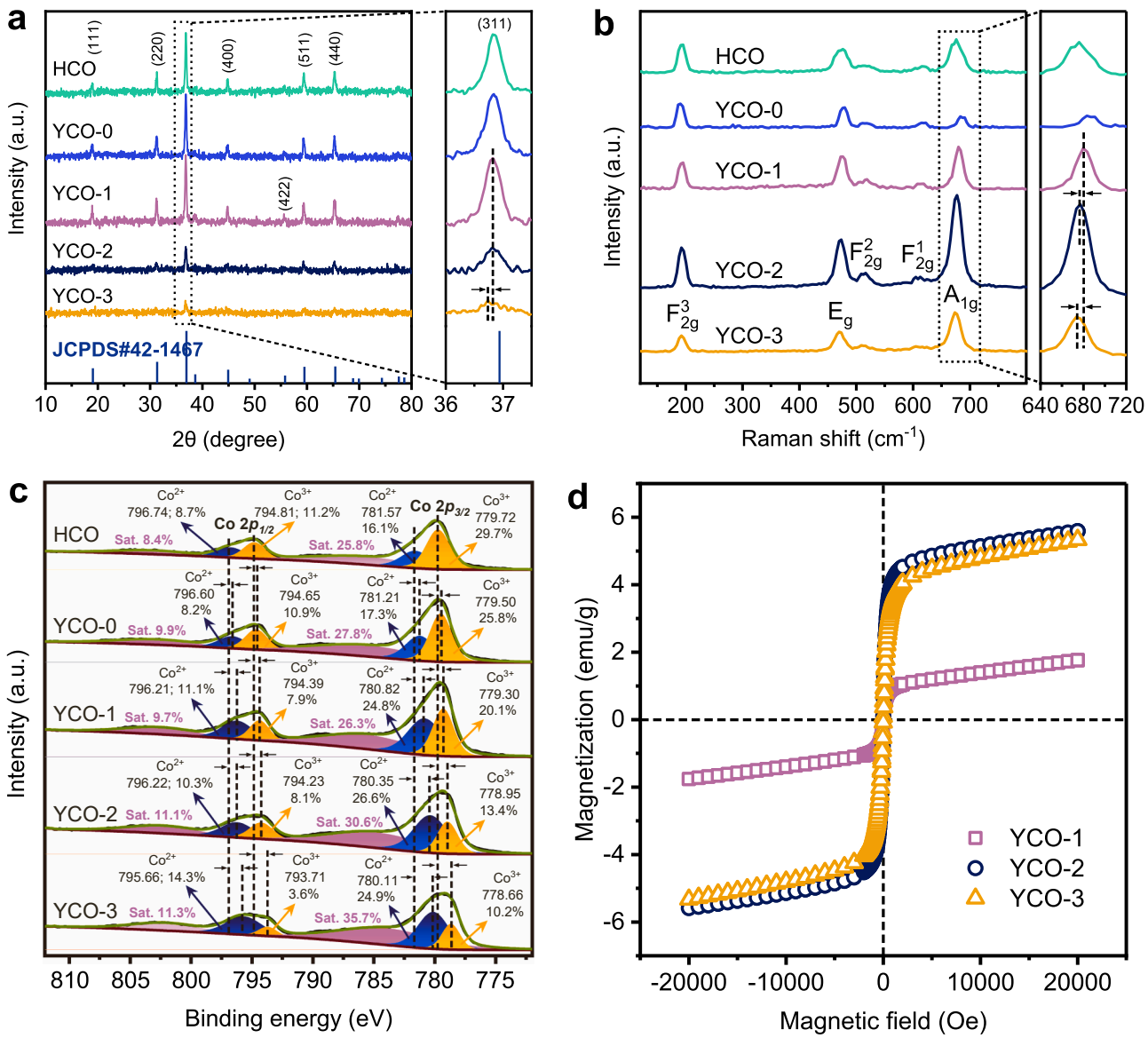

Fig. 2. (a) XRD patterns, (b) Raman spectra, and (c) Co 2*p* XPS spectra of HCO, YCO-0, and YCO-X; (d) magnetic hysteresis loops of YCO-X.

(311) crystal plane was also shifted to lower values as X increased, meaning that the d-spacing increased with X. This further provides the existence of lattice defects in YCO-X [50]. Compared to the other two of YCO-X, the peak characteristic of the (311) crystal plane of YCO-3 shifted the largest distance of ca. 0.17 (2θ degree), indicating its largest number of lattice defects. Furthermore, the microstrain of YCO-3 was also found to possess the highest value of 0.6076%, which was significantly higher than that of YCO-1 and YCO-2 with 0.4687% and 0.4933%, respectively. These results reinforce the claim of richness of lattice defects in YCO-3 compared to the others.

The Raman spectra, as seen in Fig. 2(b), further support the lattice defects. It is evident from the spectra that each catalyst had five obvious peaks. For HCO, these five peaks were identified at 195.3, 476.4, 511.3, 615.1, and 675.9 cm^{-1} characteristic of F^3_{2g}, E_g, F^2_{2g}, F^1_{2g}, and A_{1g} modes, respectively of Co_3O_4. The $F_{2\,g}$ modes were associated with the tetrahedral sites (CoO_4), while the $A_{1\,g}$ mode was related to octahedral sites (CoO_6) [51]. After reduction, these peaks revealed their downshift in YCO-X, indicating that more lattice defects were produced. In addition, the downshift degree increased with X, and the largest shift range of around 3.3 cm^{-1} was found at X equal to 3. It is accepted that lattice defects in Co_3O_4 could be either Co defects or OV. Both of them were reported to be capable of accelerating the catalytic activities due to the electron delocalization and the electron density abundance [52], [53].

To understand changes in the surface oxidation states of Co atoms with lattice defects, Co 2*p* XPR spectra were analyzed. As displayed in Fig. 2(c), HCO exhibited two peaks typical for Co $2p_{3/2}$ and Co $2p_{1/2}$ at around 779.93 and 795.03 eV, respectively [54]. Each peak consisted of Co^{2+} and Co^{3+} components. These peaks were also observed in YCO-0 and YCO-X, but their locations shifted downwards with the largest shift obtained in YCO-3. This indicates that the increase in X resulted in enhanced extent of downshift, and thereby increasing the electron density of Co atoms. Or, to put it another way, the reduction changed the region that binds to Co atoms to result in the presence of more lattice defects with the degree being enhanced as X increased. Furthermore, the increase in X also left YCO-X with high Co^{2+} percentage reflected by the ratio of Co^{2+} to (Co^{2+}+Co^{3+}) (Table 2), which is favorable for catalytic reactions due to its electron abundance [55].

As ferromagnetism is an indication of low-valent Co species, the magnetic hysteresis of YCO-X was analyzed in the range of ± 20,000 Oe (Fig. 2d). Basically, there were two characteristic parameters, including coercivity (H_C) and saturation magnetization (Ms). While H_C increased with X (0.9, 7.0, and 8.9 Oe for YCO-1, YCO-2, and YCO-3, respectively), Ms increased from 1.8 emu/g for YCO-1–5.6 emu/g for YCO-2 and then decreased to 5.3 emu/g for YCO-3. The highest H_C value of YCO-3 reflected its best external magnetic field resistance, and the magnetism in general showed a reduction of high-valent Co species to some extent. The catalytic activity, therefore, can be enhanced.

The reductivity of as-prepared catalysts were analyzed by H_2-TPR. In general, Fig. 3(a) reveals that the peak intensity representing the consumed hydrogen quantity decreased from HCO to YCO-3. This was perhaps due to the existence of more low-valent Co species of YCO-X. In particularly, YCO-3 exhibited several reduction peaks with relatively low intensity, indicating that it had a large number of electron-rich Co species in comparison with the others. On the other hand, the position of the reduction peaks also reflects the activity of a catalyst of interest. For HCO, there was an overlap of the two reduction peaks. The first peak centered at 411.26 °C represented the reduction of Co^{3+} to Co^{2+}, and the second peak at 443.03 °C represented the reduction of Co^{2+} to Co° [56]. In YCO-X, the starting point of these two peaks tended to shift towards lower temperatures as X increased. The longest shift was seen in YCO-3, suggesting that high-valent Co species of YCO-3 were likely to be reduced than those of the others. In other words, Co species in YCO-3 would be the best active sites for H_2O_2 [57].

As for the redox activity, CV curves were recorded at 60 mV/s and plotted in Fig. 3(b). Accordingly, several redox peaks with different highs were detected in the potential of 0.2264–1.6264 V vs. RHE. As the peak current density and the CV area reflect the redox activity, YCO-3 with the most abundant lattice defects exhibited the highest current density and the largest CV area, suggesting that lattice defects exerted the positive effect on speeding up the interfacial redox reaction. To infer the adsorption-controlled process, CV curves in the range of 20–100 mV/s were performed (Fig. S8), and the correlation between the square root of scan rates and current densities was established as shown in Fig. S9. It is clear that all the catalysts showed linear increases in their peak current densities with the scan rates, suggesting that the absorption-controlled process governed their kinetics behavior [38]. Furthermore, the largest slope of 1.4699 was detected for YCO-3 from the regression equation between oxidation peak current density (J_a) and the scan rates, proving the largest diffusion coefficient and consequently the fastest oxidation process of YCO-3. This could be confirmed by polarization curves in Fig. 3(c), where the current density with the lowest starting potential increased most quickly in YCO-3, whereas the opposite was true for YCO-0.

To identify the type of lattice defects, O 1 *s* XPS spectra of HCO, YCO-0, and YCO-X were analyzed. In Fig. 3(d), there were three detected peaks, consisting of surface O_{lat}, surface-adsorbed oxygen (O_{ads}), and chemisorbed oxygen-containing species, e.g., hydroxyl group [58] or water [59] ($O_{H/W}$). As O_{ads} is usually generated by the adsorption of molecular oxygen (O_2) on the active sites around OV and being activated into active oxygen species, such as superoxide (O_2^-), peroxide (O_2^{2-}), and monoatomic oxygen (O^-) [58], its presence demonstrates that OV was formed and associated with lattice defects in these catalysts. In terms of the position, all peaks of YCO-X shifted downwards in comparison with those of YCO-0, and the shift became more pronounced as X increased. As for the peak area, the $O_{H/W}$ peak had almost no change, while the O_{ads} peak increased and the O_{lat} peak decreased accordingly. Thus, it can be said that the increase in the O_{ads} peak area was resulted from the corresponding decrease in the O_{lat} peak area. Then, the ratio of O_{ads} to ($O_{H/W}$ + O_{lat}) was calculated to evaluate the OV content. Table 2 shows that this ratio increased gradually from 0.54 in HCO to 2.22 in YCO-3, quite consistent with the trend in lattice defects as revealed by XRD patterns and Raman spectra. In addition, the EPR spectra in Fig. 3(e) further display that the peak intensity followed the order of HCO < YCO-0 < YCO-1 < YCO-2 < YCO-3. As the intensity is positively correlated to the number of OV [19], the highest intensity of YCO-3 demonstrated it's the most abundance of OV. Therefore, it is argued that the abundance of OV could make YCO-3 have the most superior catalytic activity.

Finally, the effect of OV on the oxygen mobility could be examined by O_2-TPD. From Fig. 3(f), it is apparent that HCO, YCO-0, and YCO-1 had two oxygen desorption peaks (α_2 and α_3 for HCO, α_1 and α_2 for YCO-0 and YCO-1), while four obvious peaks (α_1-α_4) were detected in YCO-2 and YCO-3. The α_1 peak is usually associated with physically adsorbed O_2. The α_2 peak has to do with chemically adsorbed oxygen species (O^-, O_2^-, and O_2^{2-}) on the surface. The α_3 and α_4 peaks, meanwhile, are related to oxide (O^{2-}) of the surface O_{lat} and bulk O_{lat}, respectively [15]. Compared to HCO, which had only two peaks α_2 and α_3, the higher OV in YCO-0 made the α_1 peak appeared at a relatively low temperature of approximately 142.79 °C. Further increasing OV,

Table 2
XPS analytical results of HCO, YCO-0, and YCO-X.

Catalyst	Co 2*p* and O 1 *s* percentage (%)					Peak area ratio	
	Co^{2+}	Co^{3+}	O_{lat}	O_{ads}	$O_{H/W}$	Co^{2+}/(Co^{2+}+Co^{3+})	O_{ads}/($O_{H/W}$ + O_{lat})
HCO	24.9	40.9	42.6	35.2	22.2	0.38	0.54
YCO-0	25.5	36.7	48.5	47.0	4.5	0.41	0.89
YCO-1	35.9	28.1	41.8	53.3	4.9	0.56	1.14
YCO-2	36.9	21.5	33.6	60.3	6.1	0.63	1.52
YCO-3	39.2	13.8	26.5	68.9	4.6	0.74	2.22

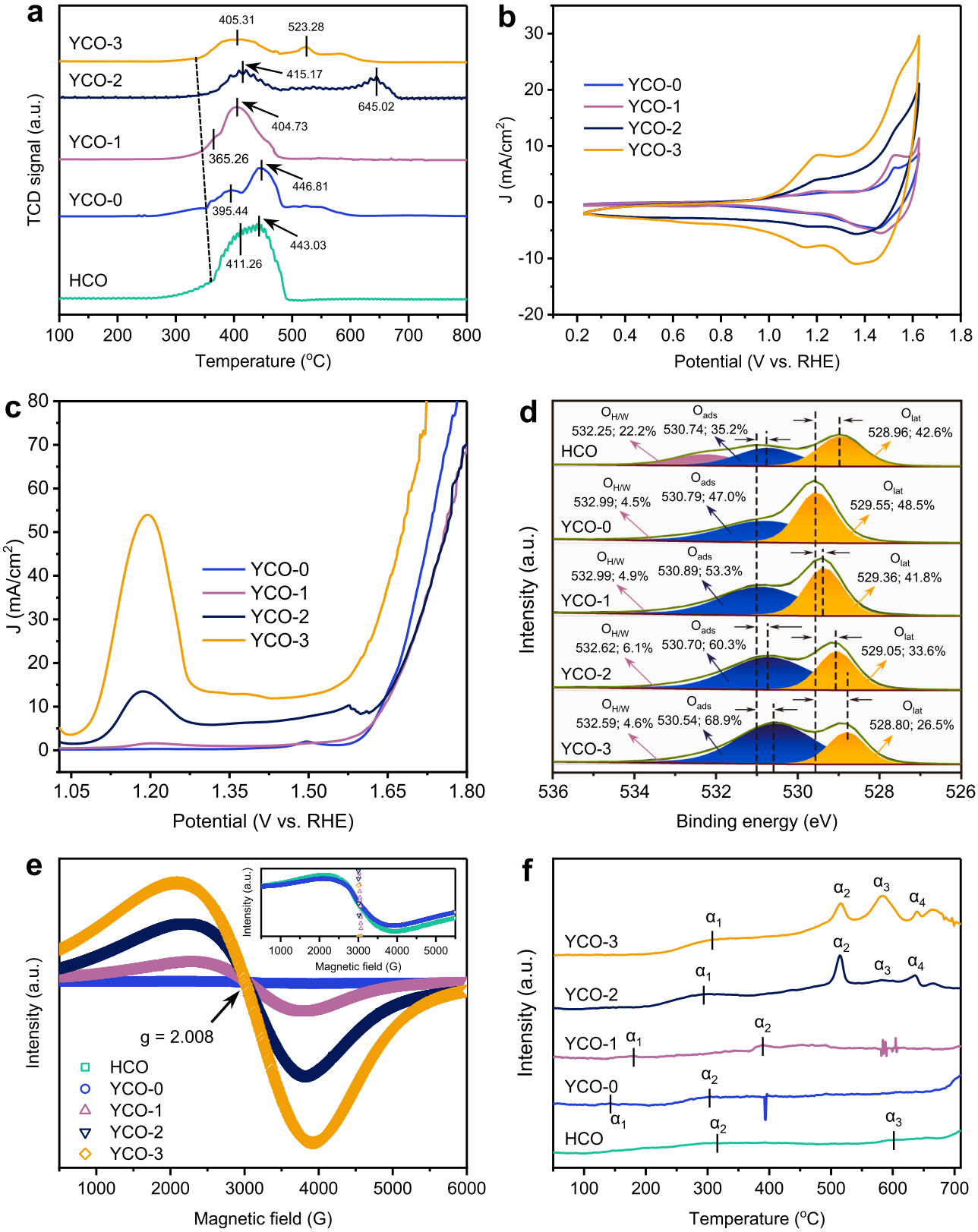

Fig. 3. (a) H_2-TPR profiles, (b) CV curves at 60 mV/s, (c) polarization curves at 5 mV/s, (d) O 1 *s* XPS spectra, (e) EPR spectra, and (f) O_2-TPD profiles of HCO, YCO-0, and YCO-X.

this peak shifted upwards from 180.54 °C in YCO-1–307.70 °C in YCO-3. Similarly, the same trend was also witnessed for the α_2 peak with the intensity increasing with OV. Besides, two more peaks α_3 and α_4 with different intensities happened to emerge at comparatively high temperatures of over 550 °C when OV content was high. Therefore, it is likely that the increase in OV raised the peak position to higher temperatures and elevated the intensity at the same time. Higher intensity and more desorption peaks mean that YCO-3 had more active oxygen species adsorbed on the surface, or rather higher OV, in line with EPR and O 1 *s* XPS spectra.

3.2. *Effects of OV on the electronic structure of YCO-X*

To investigate effects of OV on the electronic structure of YCO-X, DFT calculations were performed on Co_3O_4 (220) planes with different OV contents. The corresponding optimized structures were shown in Fig. 4 (a-c). These planes were constructed from a (1 × 2) supercell with five layers of 84 atoms in total. In the Co_3O_4 (220) plane with 1 OV (Fig. 4b), one oxygen atom was removed from the top layer. On the other hand, the Co_3O_4 (220) plane with 2 OV (Fig. 4c) was constructed from the Co_3O_4 (220) plane with 1 OV and another oxygen atom was removed from another site.

The electron density maps of these planes are shown in Fig. 4(d-f). Compared to the Co_3O_4 (220) plane without OV, the electron density of

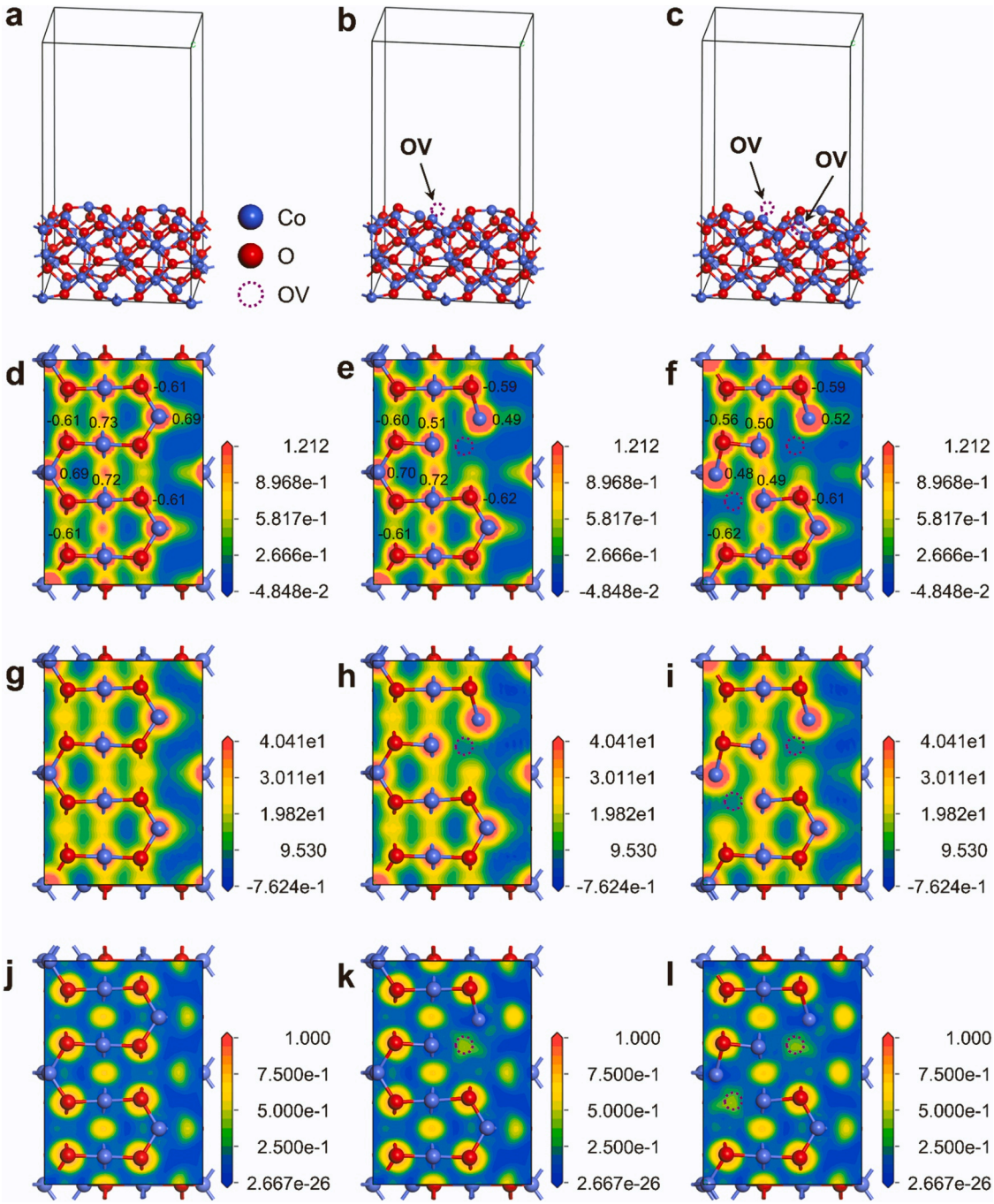

Fig. 4. (a-c) Optimized structures; (d-l) 2D top views of (d-f) electron density (the numbers noted are Mulliken charges), (g-i) SCF local potential, and (j-l) ELF of Co_3O_4 (220) planes (a, d, g, j: without OV; b, e, h, k: with 1 OV; and c, f, i, l: with 2 OV).

Co sites around OV where oxygen atom(s) were removed in the Co_3O_4 (220) planes with 1 and 2 OV increased significantly, revealing that the electron density of Co sites can be enhanced with OV. This is consistent with XPS results (Fig. 2c). Further, Mulliken charges obtained from the population analysis show that the OV introduction decreased the charges of Co sites around OV, indicating that more Co sites in the low oxidation state could be created when more OV was introduced. These Co sites were reported to have high catalytic performance [60], [61]. Similar results were also found for self-consistent field (SCF) local potential (Fig. 4g-i), which is associated with the electrostatic potential (ESP). It is known that ESP reflects the degree of electrostatic interaction between molecules with opposite potentials. Therefore, sites with large or small ESP values are considered potential for enhanced electrostatic interactions. Since the positive ESP of the H_2O_2 molecule was mainly concentrated on the two H atoms (Fig. S10), the two O atoms with negative ESP would be easily attracted to Co sites with positive ESP.

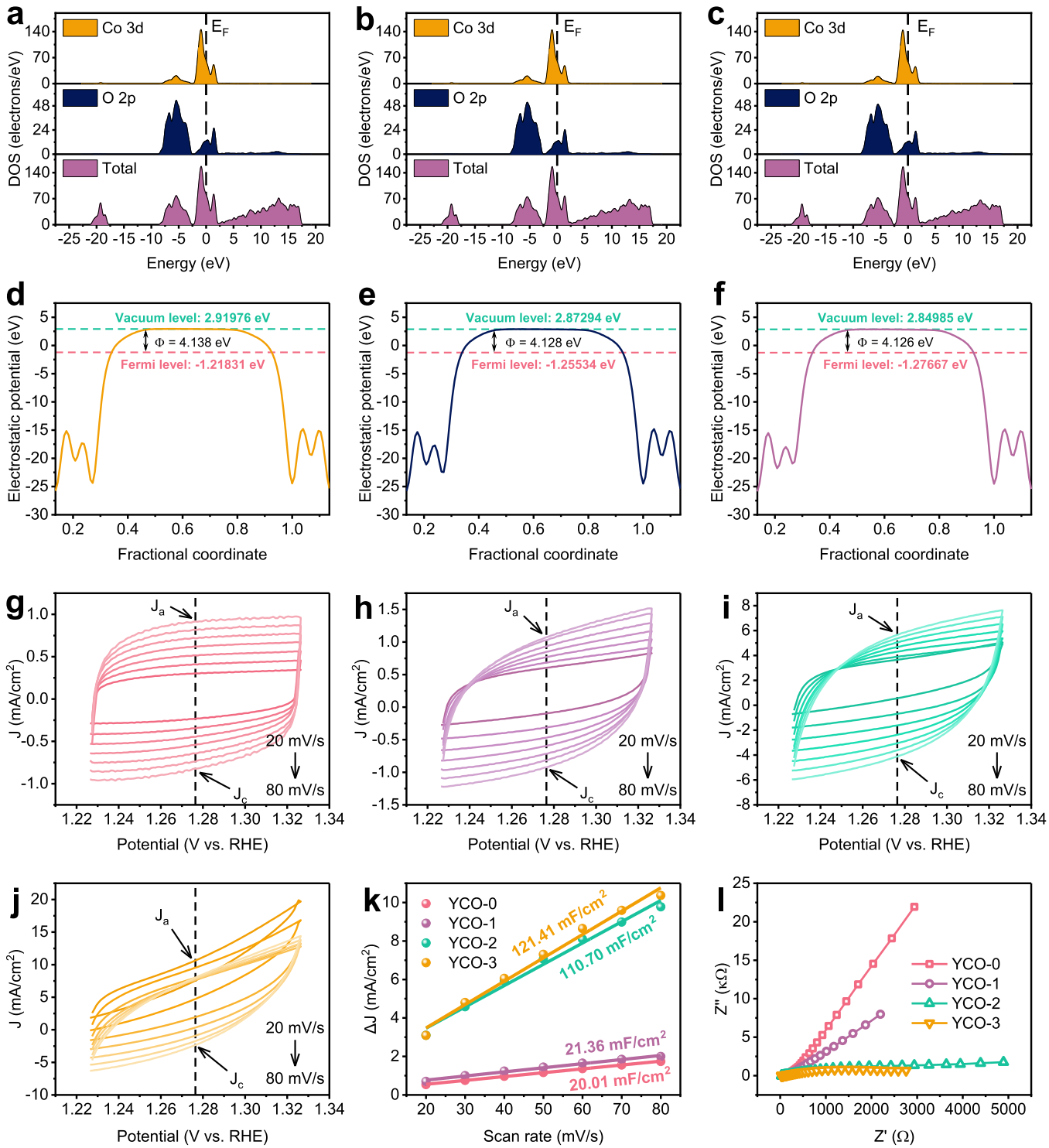

Fig. 5. (a-c) DOS and (d-f) work function of (a, d) Co_3O_4 (220) plane without OV, (b, e) Co_3O_4 (220) plane with 1 OV, and (c, f) Co_3O_4 (220) plane with 2 OV; (g-j) CV curves at different scan rates of 20–80 mV/s in a non-faradaic reaction region (1.2264 ~ 1.3264 V vs. RHE) and (k) corresponding C_{dl} values of YCO-0 and YCO-X; and (l) EIS plots at 0.5 V of YCO-0 and YCO-X in 0.5 M Na_2SO_4.

Fig. 4(g-i) depict that these Co sites became more attractive for H_2O_2 upon introducing OV. As the electron localization function (ELF) is a measure for the localization of electrons, the larger the ELF, the more electrons are localized. According to ELF maps in Fig. 4(j-l), the area with more delocalized electrons appeared at Co sites around OV, meaning that covalent bonds between Co and other O atoms around OV became weaker. Therefore, Co sites with more delocalized electrons were more active and easily to take part in reactions by donating their local electrons [62].

3.3. OV-enhanced electronical conductivity of YCO-X

As demonstrated above, the increase of OV reduced the charges of the Co sites around OV, while increasing the local electron density and the delocalization of Co sites. Therefore, it is expected that the conductivity will increase accordingly. To verify such an intrinsic property, density of states (DOS) of the Co_3O_4 (220) planes with different OV contents were calculated. As represented in Fig. 5(a-c), almost no significant difference was discerned between the electronic states of Co 3*d*, O 1 *s*, and total of the planes. This is quite unusual and contrasts with the change in the electron density of Co sites. The limitation and inadequacy of the calculation method using the Perdew-Burke-Ernzerhof (PBE) functional could be a reason [63]. Another evidence, such as work function, could be useful in this case. This is defined as the minimum energy needed for an electron to be transferred from the Fermi level into a vacuum, and is calculated using the following equation:

$$\phi = E_{vac} - E_f \tag{5}$$

where E_{vac} and E_f represent the potential at vacuum and Fermi level, respectively.

According to the results in Fig. 5(d-f), as OV increased, both vacuum and Fermi levels decreased but the decreasing rate of the Fermi level was faster. Therefore, the work function was observed to decrease as well, which was 4.138, 4.128, and 4.126 eV for the Co_3O_4 (220) planes without OV, with 1 OV, and with 2 OV, respectively. The decrease in work function with OV made electrons in YCO-X able to escape more easily, and thereby contributing to enhanced electron-donating capacity of Co sites in YCO-X with higher OV. At the same time, the enhanced electron-donating capacity also means the improved electrical conductivity, which could come from plentiful electrochemical active surface area (ECSA) as assessed by the double layer capacitance (C_{dl}) obtained via CV curves in a non-faradaic reaction region (Fig. 5g-j) [64]. The C_{dl} values (F/cm^2) of YCO-0 and YCO-X were calculated from the slope of the following linear equation and displayed in Fig. 5(k).

$$\Delta J = C_{dl} \times \upsilon + b \tag{6}$$

where ΔJ (mA/cm^2) is the average value of $J_a - J_c$, υ is the scan rate, and b is the constant.

Accordingly, the C_{dl} value increased gradually from 20.01 mF/cm^2 in YCO-0 with the lowest OV to 121.41 mF/cm^2 in YCO-3 with the largest OV, which enabled YCO-3 to possess the most plentiful ECSA of 214.55 cm^2 based Eq. (7):

$$ECSA = S \times C_{dl}/C_s \tag{7}$$

where S and C_s represent the area of the working electrode and the ideal electrode's specific capacitance, respectively. $S = \pi \times 0.3^2/4$ cm^2 and $C_s = 40 \times 10^{-3}$ mF/cm^2 in 1 M KOH.

Finally, the improved electrical conductivity was confirmed by electrochemical impedance spectroscopy (EIS) in Fig. 5(l). The semicircle radius represents the degree of impedance for the charge transfer. The smaller this radius, the lower the impedance [65]. Therefore, YCO-3 had the lowest impedance, i.e., the highest electrical conductivity. At the same time, the conductivity of the rest counterparts was determined to be in the order of YCO-0 < YCO-1 < YCO-2, good agreement with the increase in OV. In summary, the existence of OV in the crystal structure was demonstrated experimentally and theoretically to have a positive contribution to increasing the local electron density, reducing the atomic charges, increasing the delocalization of Co sites around OV, thereby reducing the work function, increasing the ECSA, and increasing the conductivity. All these factors are predicted to be able to enhance the catalytic activity and effectively direct the H_2O_2 activation.

3.4. Evaluation of the catalytic performance for SDZ degradation and H_2O_2 activation

Fig. 6(a) compares the SDZ degradation in different systems. It is clearly that YCO-3 could not adsorb SDZ, and H_2O_2 could not degrade SDZ by itself. Meanwhile, SDZ could be degraded to some extent by the combination of H_2O_2 with any catalysts. By comparison, YCO-0 demonstrated its higher performance than HCO, suggesting that surface area played a certain role in enhancing the performance. When OV was created, the performance was further enhanced. Among YCO-X, YCO-3 had the best performance. To calculate the rate constant (k_{obs}), two kinetic reaction equations were adopted. Based on the calculated data in Table S3-S7, the SDZ degradation followed the second order reaction and was illustrated as a plot of $1/C_t$ (mM^{-1}) vs t (min) in Fig. 6 (b). Because YCO-3 was the most powerful catalyst, it had the highest k_{obs} of 4.1476 mM^{-1}min^{-1} for SDZ degradation, while lowest k_{obs} of 0.0574 mM^{-1}min^{-1} was for HCO.

Fig. 6(c) illustrates the H_2O_2 consumption in different systems, which was directly proportional to the SDZ degradation rate. The more activated H_2O_2, the higher the efficiency of SDZ degradation. The activation of H_2O_2 by these catalysts followed the pseudo first order reaction (Table S8-S12), which was fitted by linear equations as shown in Fig. 6 (d). Obviously, those catalysts with higher H_2O_2 consumption performance would have higher H_2O_2 consumption rate constants, which followed the order of HCO < YCO-0 < YCO-1 < YCO-2 < YCO-3.

The reasons for these results are believed to come from the synergetic effects of different factors, for example surface area, pore volume, pore radius, microstrain, crystallite size, Co^{2+} content, and OV content because these factors change with the change in OV. Fig. 6(e-k) show the relationship between these factors with k_{obs} for the SDZ degradation. It is observed that k_{obs} increased with surface area, pore volume, microstrain, Co^{2+} content, and OV content as against pore radius and crystallite size. Compared to other factors, surface area, Co^{2+} content, and OV had the best fit with R^2 of 0.9996, 0.9838, and 0.9711, respectively, suggesting that the combination of these three factors boosted the activation of H_2O_2 and SDZ degradation afterwards.

3.5. Degradation of SDZ under different conditions and YCO-3 reusability

To evaluate the performance for SDZ degradation under different conditions, several experiments were conducted in YCO-3/H_2O_2 system. Fig. 7(a) depicts that SDZ degradation was not influenced much by YCO-3 amount in the range of 100–200 mg/L with a slightly increased k_{obs} from 3.5534 mM^{-1}min^{-1} at 100 mg/L to 4.2233 mM^{-1}min^{-1} at 200 mg/L (inset), but the efficiency decreased when the YCO-3 amount was 50 mg/L. The corresponding k_{obs} was 1.2012 mM^{-1}min^{-1}, revealing the insufficient active sites. As for H_2O_2 concentration (Fig. 7b), the increase from 30 to 90 mM enhanced the degradation efficiency with the k_{obs} of 1.2436–4.1476 mM^{-1}min^{-1}, respectively. However, further increasing to 120 mM, the k_{obs} dropped to 3.7269 mM^{-1}min^{-1}. This meant that the excess H_2O_2 was not favorable to the reaction, possibly because of the reverse reaction of ROS with H_2O_2 (Eqs. 8–10) [66].

$$H_2O_2 + O_2^{\cdot -} \rightarrow {}^{\cdot}OH + OH^- + O_2 \left(k = 0.13 \pm 0.07 M^{-1}s^{-1}\right) \tag{8}$$

$$H_2O_2 + {}^{\cdot}OH \rightarrow HO_2^{\cdot} + H_2O \rightleftharpoons O_2^{\cdot -} + H^+ \left(k = 2.71\acute{0}^7 M^{-1}s^{-1}\right) \tag{9}$$

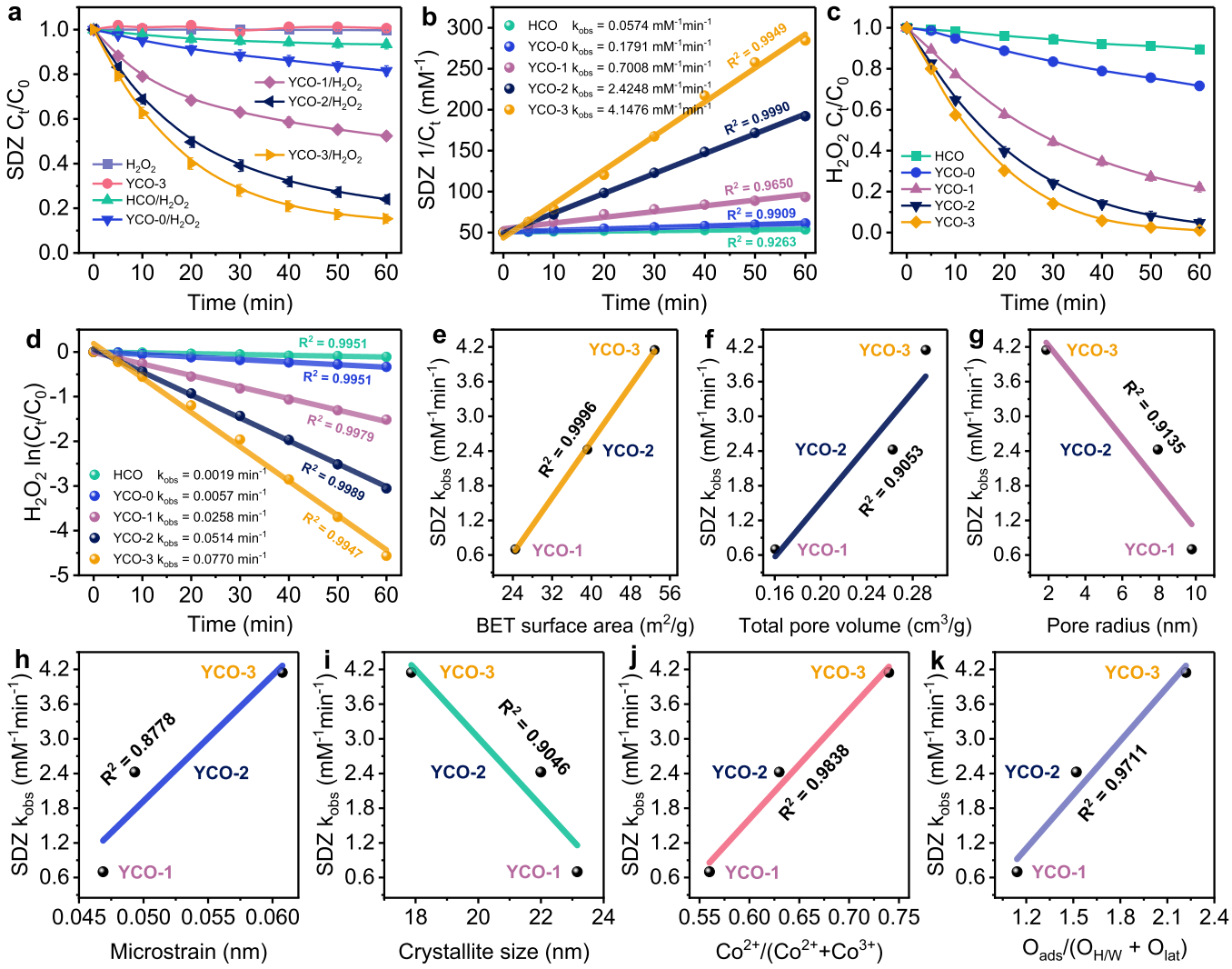

Fig. 6. (a) SDZ degradation and (b) corresponding 2nd order reaction kinetics; (c) H_2O_2 consumption and corresponding 1st order reaction kinetics (catalysts = 150 mg/L, H_2O_2 = 90 mM, SDZ = 5 mg/L, and t = 30 °C); (e-g) plots of k_{obs} vs (e) S_{BET}, (f) total pore volume, (g) pore radius, (h) microstrain, (i) crystallite size, (j) $Co^{2+}/(Co^{2+} + Co^{3+})$, and (k) $O_{ads}/(O_{H/W} + O_{lat})$.

$$HO_2^{\cdot} + {}^{\cdot}OH \rightarrow O_2 + H_2O \ (k = 6.01\acute{0}^9 M^{-1}s^{-1}) \quad (10)$$

Increase in SDZ concentration, on the other hand, had adverse effects on the performance (Fig. 7c). The higher the concentration of SDZ, the lower the degradation efficiency and the lower the reaction rate due to the increased competition for the adsorption sites with H_2O_2 and the inadequate generation of ROS. In contrast, temperature had the positive effect on the performance as the higher the temperature, the faster the reaction rate (Fig. 7d). To calculate the activation energy, the linear relationship between $\ln k_{obs}$ and 1000/T was established. By using Eq. (11), the activation (E_a) of 30.323 kJ/mol was obtained.

$$\ln k_{obs} = -E_a/RT + \ln A \quad (11)$$

where E_a is the activation energy (J/mol), R is the gas constant (8.314 J. $mol^{-1}K^{-1}$), T is the absolute temperature (K), and A is the pre-exponential factor.

In addition, effect of HA and anions was also investigated. As Fig. 7 (e) shows, the presence of either HA or anions hindered the SDZ degradation to some extent. The most obvious effect was observed for HA with k of 2.3255 $mM^{-1}min^{-1}$ in contrast to the least effect caused by HCO_3^- with k of 3.1794 $mM^{-1}min^{-1}$. In general, the effect by HA was mainly due to its competition for the adsorption sites, while the reaction of anions with ROS accounted for the reduced performance. As pH is a factor affecting the degradation efficiency [67], its effect was examined in Fig. 7(f) for SDZ degradation and in Fig. 7(g) for H_2O_2 consumption. It is apparent from Fig. 7(f) that the most obvious effects were seen at pH 3 and pH 11. While pH 11 accelerated the SDZ degradation, the performance was reduced at pH 3. At pH in the range of 5–9, the performance did not verify too much. Similar trend was also observed for the H_2O_2 consumption in Fig. 7(g) and Fig. S12, suggesting that the interaction between YCO-3, H_2O_2, and SDZ determined the SDZ degradation performance. At low pH, the abundance of H^+ could react with either $O_2^{\bullet -}$ via Eq. (12) or $^{\bullet}OH$ via Eq. (13), thereby lowering the degradation efficiency.

$$H^+ + O_2^{\cdot -} + HO_2^{\cdot} \rightarrow H_2O_2 + O_2 \ (k = 81\acute{0}^7 M^{-1}s^{-1}) \quad (12)$$

$$H^+ + {}^{\cdot}OH + e^- \rightarrow H_2O \quad (13)$$

Furthermore, H_2O_2 and SDZ mainly existed in the form of $H_3O_2^+$ (Fig. 7 h) and SDZ^+ (Fig. 7i) at pH 3, respectively, while YCO-3 was positively charged at all pH values. Thus, the electrostatic repulsion between them could be another cause for the decline in the performance. In contrast, because H_2O_2 existed in the form of both $H_3O_2^+$ and HO_2^-, and SDZ^- was the predominant form of SDZ at pH 11, the electrostatic attraction between the positively charged YCO-3 and these two above

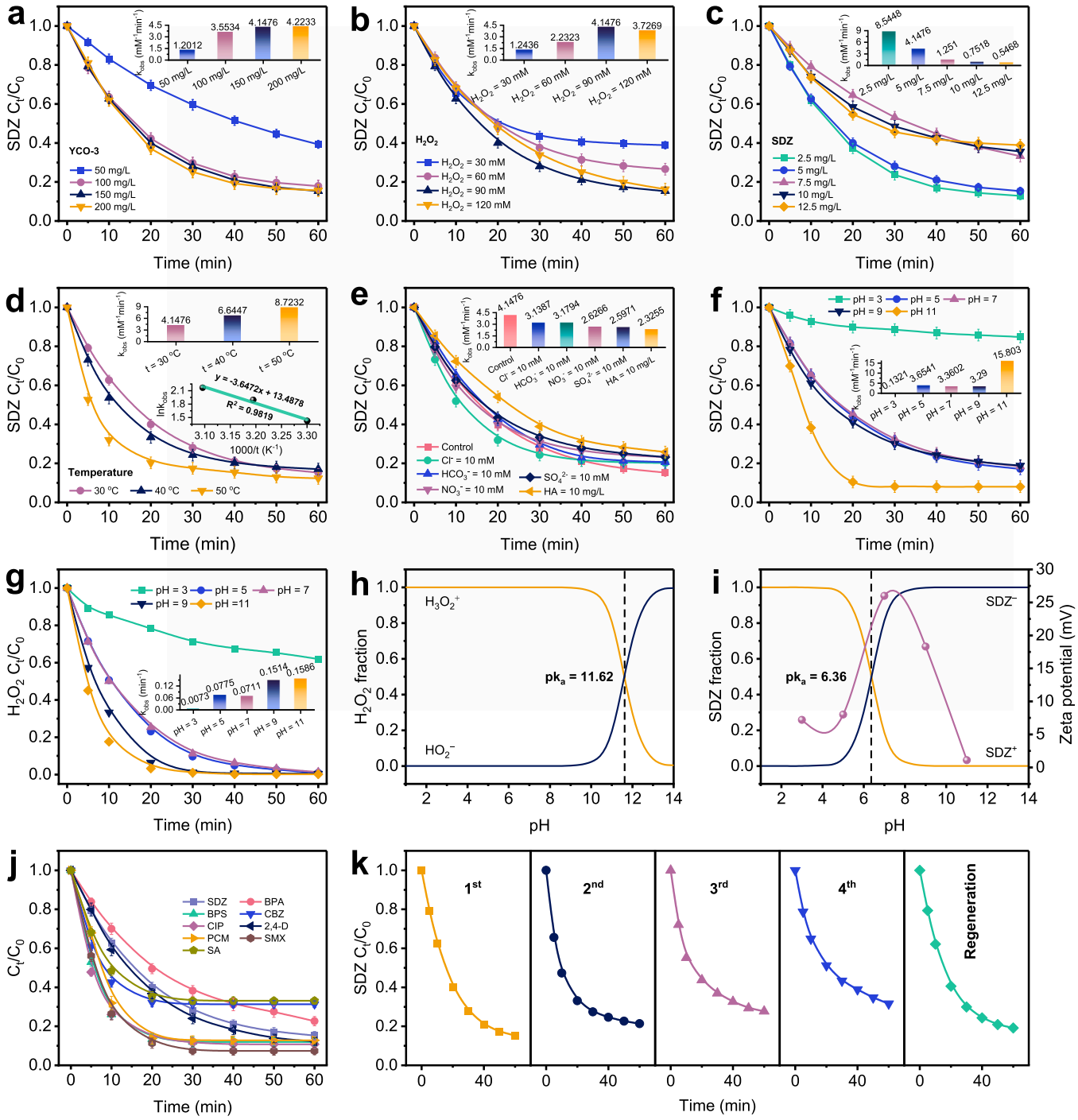

Fig. 7. (a-f) effects of (a) YCO-3 amount, (b) H_2O_2 concentration, (c) SDZ concentration, (d) temperature, (e) anions and HA, and (f) pH on SDZ degradation; (g) effect of pH on H_2O_2 consumption; (h) variation of H_2O_2 species at different pH; (i) variation of SDZ species at different pH and zeta potential of YCO-3; (j) different pollutants-degrading performance in YCO-3/H_2O_2 system; and (k) reusability of YCO-3 for SDZ degradation (YCO-3 = 150 mg/L, H_2O_2 = 90 mM, SDZ = pollutants = 5 mg/L, and t = 30 °C).

components promoted the degradation efficiency. To test the applicability of YCO-3/H_2O_2 system, the degradation of several emerging pollutants, including endocrine disrupting chemicals (bisphenol A, BPA; bisphenol S, BPS), pharmaceutical and personal care products (carbamazepine, CBZ; paracetamol, PCM), fluoroquinolone antibiotic (CIP), sulfonamide antibiotics (sulfamethoxazole, SMX; sulfanilamide SA), and herbicide (2,4-dichlorophenoxyacetic acid, 2,4-D) were investigated. As can be seen in Fig. 7(j), BPS, CIP, 2.4-D, PCM, and SMX could degrade more than 80% within 60 min, while the degradation of BPA, CBZ, and SA reached 77.4%, 68.7%, and 66.9%, respectively at the end of the reaction. These results indicate that the YCO-3/H_2O_2 system exhibited high efficiency for the degradation of different pollutants. Finally, the stability of YCO-3 was evaluated via four-consecutive cycle reusability. The results in Fig. 7(k) demonstrate that YCO-3 remained performance for SDZ degradation over four cycles with slight decreases and the performance after regeneration was even comparable to that in the first cycle, suggesting that YCO-3 was very stable. This was probably due to its strength in the crystal structure [68], no change in elemental composition, and increase in OV content after regeneration (Fig. S13).

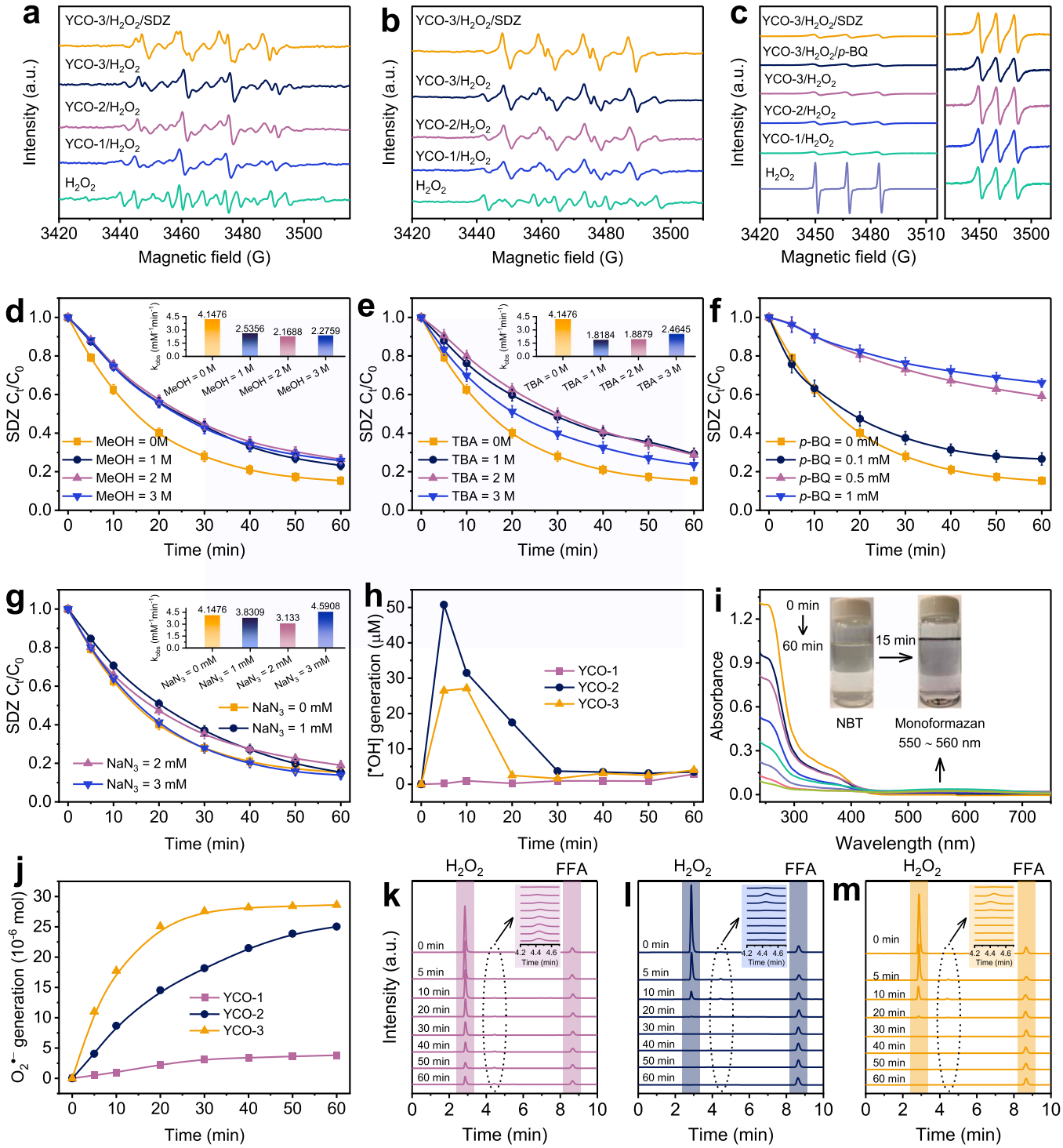

Fig. 8. (a-c) EPR spectra of (a) DMPO- $^{\bullet}$OH, (b) DMPO-$O_2^{\bullet-}$, (c) TEMPO; (d-g) effects of scavengers on SDZ degradation in YCO-3/H_2O_2 system; (h) generation of $^{\bullet}$OH; (i) UV–vis spectra of NBT reduction by $O_2^{\bullet-}$ generated in YCO-3/H_2O_2 system (insets are NBT solution (left) and NBT solution filtrate after 15 min of reaction (right)); (j) generation of $O_2^{\bullet-}$; and (k-m) FFA chromatograms in (k) YCO-1/H_2O_2, (l) YCO-2/H_2O_2, and (m) YCO-3/H_2O_2 systems (YCO-X = 150 mg/L, H_2O_2 = 90 mM, SDZ = 5 mg/L, BA = FFA = 0.2 mM, NBT = 65 mg/L, and t = 30 °C).

3.6. EPR analyses, quenching experiments, and ROS generation

ROS generated in the Fenton-like process driven by YCO-X/H_2O_2 was first detected by EPR analyses using two spin-trapping agents, including 5,5-dimethyl-pyrroline *N*-oxide (DMPO, for $^{\bullet}$OH and $O_2^{\bullet-}$) and 2,2,6,6-tetramethylpiperidine (TEMP, for $^1O_2$). As shown in Fig. 8(a), several signals of DMPO-$^{\bullet}$OH were observed. These signals were slightly intensified by the combination of YCO-X with H_2O_2 than those by only H_2O_2, enunciating that H_2O_2 was activated by YCO-X to form $^{\bullet}$OH with a little amount. In Fig. 8(b), DMPO-$O_2^{\bullet-}$ signals of YCO-X/H_2O_2 were higher than those of H_2O_2, and the intensity increased from YCO-1 to YCO-3, manifesting that the increase of OV enhanced the generation of $O_2^{\bullet-}$. Unlike $^{\bullet}$OH and $O_2^{\bullet-}$, it would seem that $^1O_2$ was not generated by YCO-X/H_2O_2 because 2,2,6,6-tetramethylpiperidine-*N*-oxyl (TEMPO) signals assigned to a TEMP-$^1O_2$ adduct [69] were substantially alleviated when H_2O_2 was combined with YCO-X (Fig. 8c). The magnified

spectra on right hand side show that the intensity increased with OV, but was too low in comparison with H_2O_2, implying that $^1O_2$ was actually generated by YCO-X/H_2O_2 but negligibly. Upon combination with *p*-BQ, the intensity of YCO-3/H_2O_2 was reduced, signifying that $^1O_2$ might be generated from $O_2^{\bullet-}$ [70] (Eq. 14-17).

$$O_2^{\cdot-} + HO_2^{\cdot} \rightarrow {}^1O_2 + HO_2^{-} \tag{14}$$

$$O_2^{\cdot-} + 2H_2O \rightarrow {}^1O_2 + H_2O_2 + 2OH^- \tag{15}$$

$$2O_2^{\cdot-} + 2H^+ \rightarrow {}^1O_2 + H_2O_2 \ (k < 0.2\ M^{-1}s^{-1}) \tag{16}$$

$$O_2^{\cdot-} + {}^{\cdot}OH \rightarrow {}^1O_2 + OH^- \left(k = 81\acute{0}^9 M^{-1}s^{-1}\right) \tag{17}$$

Overall, $O_2^{\bullet-}$ was more likely than $^{\bullet}OH$ to generate by YCO-X/H_2O_2, while the generation of $^1O_2$ was neglectable. To realize their contribution in the SDZ degradation, ROS-capturing experiments were performed. With a high reaction rate of $9.7 \times 10^8\ M^{-1}s^{-1}$ with $^{\bullet}OH$ for MeOH and 3.8–7.6 × $10^8\ M^{-1}s^{-1}$ with $^{\bullet}OH$ for TBA [71], these two scavengers were used to quench $^{\bullet}OH$. As can be seen from results in Fig. 8(d, e) that the presence of either MeOH or TBA with increasing the concentration did not reduce the degradation of SDZ to a higher extent, proving the marginal role of $^{\bullet}OH$. Meanwhile, an enhancement in the suppression of SDZ degradation was observed as the scavenger for $O_2^{\bullet-}$, *p*-BQ ($k = 1.2 \times 10^9\ M^{-1}s^{-1}$), with a higher concentration was employed (Fig. 8 f), showing that the role of $O_2^{\bullet-}$ in the degradation of SDZ could not be ignored. For NaN_3, a scavenger for $^1O_2$ ($k = 1.0 \times 10^9\ M^{-1}s^{-1}$) [72], it is not too surprising that no obvious inhibition occurred even when the concentration of the added NaN_3 was increased (Fig. 8 g). This was in full agreement with the EPR results, further signifying a negligible role of $^1O_2$. To find out whether there would be any shift in the SDZ degradation mechanism occurred, the same ROS-capturing experiments were performed for YCO-1 and YCO-2 with lower OV. However, the results in Fig. S14 show that the role of each ROS in YCO-1/H_2O_2 and YCO-2/H_2O_2 systems was quite similar to that of each ROS in YCO-3/H_2O_2 system despite the change in OV content. The inhibition against the degradation of SDZ due to FFA, a well-known scavenger for $^1O_2$ with a rate constant of $1.2 \times 10^8\ M^{-1}s^{-1}$, could come from its acceleration in the consumption of H_2O_2. Therefore, it can be said that $O_2^{\bullet-}$ was generated by YCO-X-activated H_2O_2, enhanced by OV, and played a significant role in the SDZ degradation.

It is reported that $O_2^{\bullet-}$ could be generated from O_2 [73,74]. If this is the case, the degradation of SDZ will be accelerated. Fig. S15 shows that N_2 purging resulted in reduced SDZ degradation, signifying that dissolved oxygen (DO) may, to a certain extent, be responsible for producing $O_2^{\bullet-}$. To confirm this, O_2 purging was further conducted. The result will be better if DO indeed participates in the SDZ degradation. However, the degradation was not enhanced, indicating an insignificant role of DO in the generation of $O_2^{\bullet-}$.

The generation of the above ROS was further measured to evaluate the ability to activate H_2O_2 of the Fenton-like system by YCO-X. Quantitative experiments with BA, NBT, and FFA were carried out. These probes were selected for $^{\bullet}OH$, $O_2^{\bullet-}$, and $^1O_2$ with rate constant of 4.3×10^9, 5.76–6.04 × 10^4, and $1.2 \times 10^8\ M^{-1}s^{-1}$, respectively [75, 76]. As depicted in Fig. 8(h), the generation of $^{\bullet}OH$ via measurement of the produced *p*-HBA [61] in Fig. S16 was different between these YCO-X. Increasing OV led to higher $^{\bullet}OH$ generation, but the generation was not continuous and rather diminished as the time carried on. This suggests that $^{\bullet}OH$ was enhanced by OV and might have been involved in some reactions in which it was an intermediate. Meanwhile, $O_2^{\bullet-}$ was quantified by the reduction of NBT via single-electron transfer reaction to form monoformazan as an indication at around 550–560 nm on the UV–vis spectra [77]. Take the YCO-3/H_2O_2 system as an example, insets of Fig. 8(i) show that yellow color of the NBT solution before reaction transformed into purple after 15 min of reaction. In addition, the maximum absorption peak of NBT at 259 nm decreased over time, and a new peak at around 550–560 nm typical for the monoformazan increased simultaneously, implying that $O_2^{\bullet-}$ was actually generated by YCO-3/H_2O_2 to reduce NBT. Then, the generation of $O_2^{\bullet-}$ in YCO-X/H_2O_2 systems based on the reduction of NBT in Fig. S17 was compared together. It is clear from Fig. 8(j) that $O_2^{\bullet-}$ was generated and increased with OV, good in accord with the results from quenching experiments and EPR analyses, thereby demonstrating that $O_2^{\bullet-}$ was the main species accounting for SDZ degradation. The loss of FFA by $^1O_2$ further support this claim as very little FFA was consumed (Fig. 8k-m) and a new peak at roughly 5 min (insets), which was ascribed to the transformation product of FFA via reaction with $^1O_2$ [78], was generated limitedly and decreased over time when increasing OV.

3.7. Electron transfer-mediated enhancement of $O_2^{\bullet-}$ generation and mechanism exploration

In order to exhaustively consider whether or not other reactive species, such as high-valent Co-oxo species [Co(IV)=O] and surface-bound radicals, were produced, effects of DMSO and KI on SDZ degradation were investigated. Firstly, almost no change in SDZ degradation, as shown in Fig. 9(a), suppressed the possibility of Co(IV)=O being produced [79] as DMPO can react with Co(IV)=O at a high reaction rate constant of $2.4 \times 10^6\ M^{-1}s^{-1}$ [80]. This was further evidenced by the absence of methyl phenyl sulfone ($PMSO_2$) in Fig. S18 as a result of the reaction between methyl phenyl sulfoxide (PMSO) and such a species ($k = 2.0 \times 10^6\ M^{-1}s^{-1}$) via an oxygen atom transfer [80]. Next, no inhibition caused by KI was observed in Fig. S19, ruling out the participation of surface-bound radicals in the degradation of SDZ [61].

The generation of ROS could be resulted from the activation of H_2O_2 by catalysts in the absence of pollutant(s), whereas the electron transfer-mediated reaction takes place when both H_2O_2 and pollutant(s) take part simultaneously in the reaction. Such a pathway has been explored recently [81], making it curious to find a link between SDZ degradation and electron transfer. It is known that pollutants rather reduce the consumption of H_2O_2 in the system that has nothing to do with electron transfer, but the opposite will be true if electron transfer is present. The promoted consumption of H_2O_2, as represented in Fig. 9(b), to a larger extent by adding SDZ with increasing concentration partly demonstrated the presence of electron transfer in the YCO-3/H_2O_2 system [82]. This is perhaps the fact that SDZ acted as an electron donor decomposing the YCO-3/H_2O_2 complex. To support this argument, the redox capacity of YCO-3 was tested with CV curves with/without H_2O_2/SDZ (Fig. 9c). It is obvious that the presence of H_2O_2 made the oxidation peak increase rapidly at a quite low potential as a result of the YCO-3/H_2O_2 complex formation. When the SDZ was present afterwards, this peak decreased but was still maintained at a high current, indicating that the complex was decomposed. In contrast, the CV area decreased dramatically without generating any oxidation peak in the presence of SDZ only, proving that H_2O_2 but not SDZ can form the complex with YCO-3. As evidenced above, OV could enhance the generation of $O_2^{\bullet-}$. Therefore, it is necessary to compare complex-forming capacity in YCO-X/H_2O_2/SDZ systems, which is usually recognized by the degree of variation of the current or potential when adding an oxidant followed by a pollutant. As a result, Fig. 9(d, e) show that YCO-X with higher OV could form a stronger metastable YCO-X/H_2O_2 complex. The sudden drops in the current or the rises in the potential upon addition of H_2O_2 were due to the redistributed electron density of YCO-X when forming complexes with H_2O_2 [83], while the second negative current or potential responses were caused by electrons transferring from SDZ to the adsorbed H_2O_2. By this way, SDZ was oxidized and H_2O_2 was reduced simultaneously. In addition, the variation to a larger extent when adding SDZ of YCO-3 suggested more electrons from SDZ transferred to H_2O_2 to result in more H_2O_2 decomposition. Therefore, it is quite reasonable to suppose that the decomposition of more H_2O_2 could lead to more $O_2^{\bullet-}$ generation. In this regard, the link between the presence of SDZ and the generation of $O_2^{\bullet-}$ was established as depicted in Fig. 9(f). As expected,

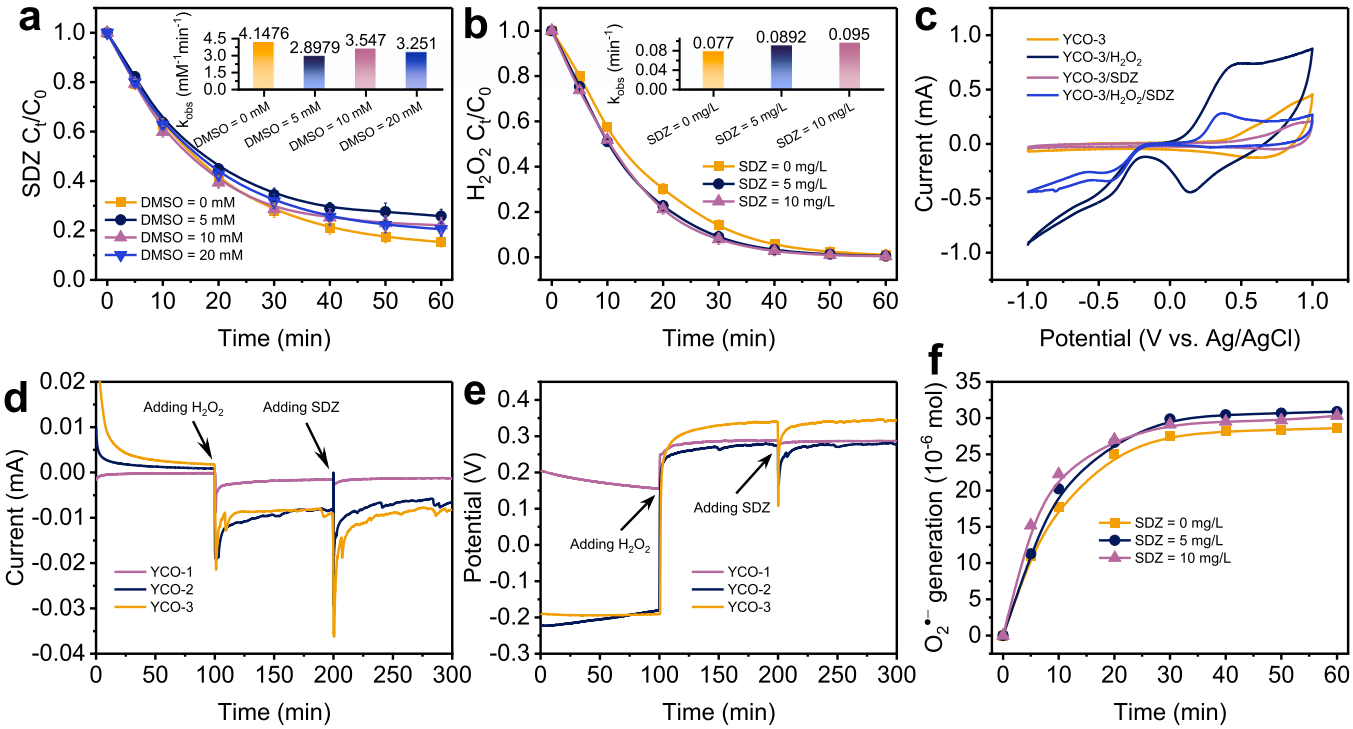

Fig. 9. (a, b) effects of (a) DMSO on SDZ degradation and (b) SDZ on H_2O_2 consumption in YCO-3/H_2O_2 system (YCO-3 = 150 mg/L, H_2O_2 = 90 mM, SDZ = 5 mg/L, and t = 30 °C); (c) CV curves at 100 mV/s of YCO-3 with/without H_2O_2, SDZ, and H_2O_2/SDZ; (d) current responses of YCO-X to the addition of H_2O_2 and SDZ; (e) OCP curves of YCO-X with the addition of H_2O_2 and SDZ; and (f) effect of SDZ on the $O_2^{\bullet-}$ generation in YCO-3/H_2O_2 system (YCO-3 = 150 mg/L, H_2O_2 = 90 mM, NBT = 65 mg/L, and t = 30 °C).

more $O_2^{\bullet-}$ was generated in the presence of higher SDZ concentration, suggesting that the generation of $O_2^{\bullet-}$ was enhanced by the electron transfer as a mediator.

To unravel the mechanism for the enhanced generation of $O_2^{\bullet-}$ medicated by the electron transfer, adsorption models of H_2O_2 on Co_3O_4 (220) planes with/without OV were simulated. To realize the role of OV, two O atoms in the H_2O_2 molecule were adsorbed onto two Co sites in the same position for all the three planes. These Co sites were located around OV in the case of Co_3O_4 (220) planes with 1 and 2 OV as these two sites were revealed to have a high local electron density regulated by OV. As a result, the optimized adsorption models of H_2O_2 on these planes were depicted in Fig. 10(a-c). As the adsorption performance is reflected by E_{ads}, the E_{ads} values of these models were calculated and the corresponding charge density differences (CDD) were visualized in Fig. 10(d-l). Accordingly, E_{ads} values of these models were negative, indicating that the adsorption processes were exothermic, and the adsorption models were stable. The more negative the E_{ads}, the higher the adsorption performance [84]. Thus, the adsorption performance of the Co_3O_4 (220) plane with 1 OV towards H_2O_2 (−5.611889 eV) was higher than that of the plane without OV (−4.218089 eV). This E_{ads} was further reduced to − 5.823289 eV as H_2O_2 was adsorbed on the Co_3O_4 (220) plane with 2 OV. Also, the O-O bond length of H_2O_2 was found to be lengthened to larger extent as OV increased. Therefore, the adsorption of H_2O_2 occurred more easily to form more $^{\bullet}OH$ on the plane with increasing OV. There would be two possible cases for the higher adsorption performance: (i) the higher H_2O_2 activation to generate more ROS and (ii) the higher catalyst/H_2O_2 complex formation ability. However, Table 3 shows that the same number of electron transferred from Co sites to H_2O_2 (0.73 e) was occurred for both Co_3O_4 (220) planes with 1 and 2 OV but lower than that for the Co_3O_4 (220) plane without OV (0.75 e), disclosing that increasing OV made the H_2O_2 activation tend to form the catalyst/H_2O_2 complex in the electron transfer pathway rather than transferring electrons to H_2O_2 for the activation to generate more $O_2^{\bullet-}$ directly. In addition, the generation of $^{\bullet}OH$ increased but was quickly depleted as the time went on (Fig. 8 h), while the generation of $O_2^{\bullet-}$ increased with OV (Fig. 8j), suggesting that the electron transfer acted as a mediator for the enhanced generation of $O_2^{\bullet-}$. In summary, the theoretical calculations and experimental results were consistent, and the increase of $O_2^{\bullet-}$ generation with OV was well demonstrated.

In short, the main mechanism for SDZ degradation in Fenton-like process driven by YCO-3/H_2O_2 was summarized in Fig. 11. YCO-3 with OV-regulated high local electron density of Co sites enabled these Co sites to be highly capable of adsorbing H_2O_2 to form the strong metastable YCO-3/H_2O_2 complex. Subsequently, YCO-3 donated partly its intrinsic electrons to H_2O_2 to form $O_2^{\bullet-}$ and limited $^{\bullet}OH$ via Eqs. (18–23) as evidenced by the change in Co species oxidation states (Fig. S20a). Meanwhile, the free O_2 molecule adsorbed on the sites where OV was present, and was activated by electrons transferred from electron-rich Co sites to form active oxygen species (O^-, O_2^-, O_2^{2-}). The formation of these species explained the variation of OV and subsequently O_{lat}, due to the oxidation of Co sites, as shown in Fig. S20(b).

$$Co^{2+} + H_2O_2 \rightarrow Co^{3+} + {}^{\cdot}OH + OH^- \quad (18)$$

$$Co^{3+} + H_2O_2 \rightarrow Co^{2+} + HO_2^{\cdot} + H^+ \quad (19)$$

$$H_2O_2 + {}^{\cdot}OH \rightarrow HO_2^{\cdot} + H_2O \rightleftharpoons O_2^{\cdot-} + H^+ \ \left(k = 2.71\acute{0}^7\ M^{-1}s^{-1}\right) \quad (20)$$

$$HO_2^{\cdot} \rightarrow H^+ + O_2^{\cdot-} \quad (21)$$

$$Co^{3+} + HO_2^{\cdot} \rightarrow Co^{2+} + O_2 + H^+ \quad (22)$$

$$Co^{2+} + {}^{\cdot}OH \rightarrow Co^{3+} + OH^- \quad (23)$$

At the same time, the metastable YCO-3/H_2O_2 complex with high potential tended to withdraw electrons from SDZ to result in H_2O_2 activation via single-electron transfer to form more $^{\bullet}OH$ (Eq. 24) whereby YCO-3 acted as an electron mediator. The generated $^{\bullet}OH$ then reacted back with H_2O_2 via Eq. (20) to form more $O_2^{\bullet-}$ (Fig. 9 f). This

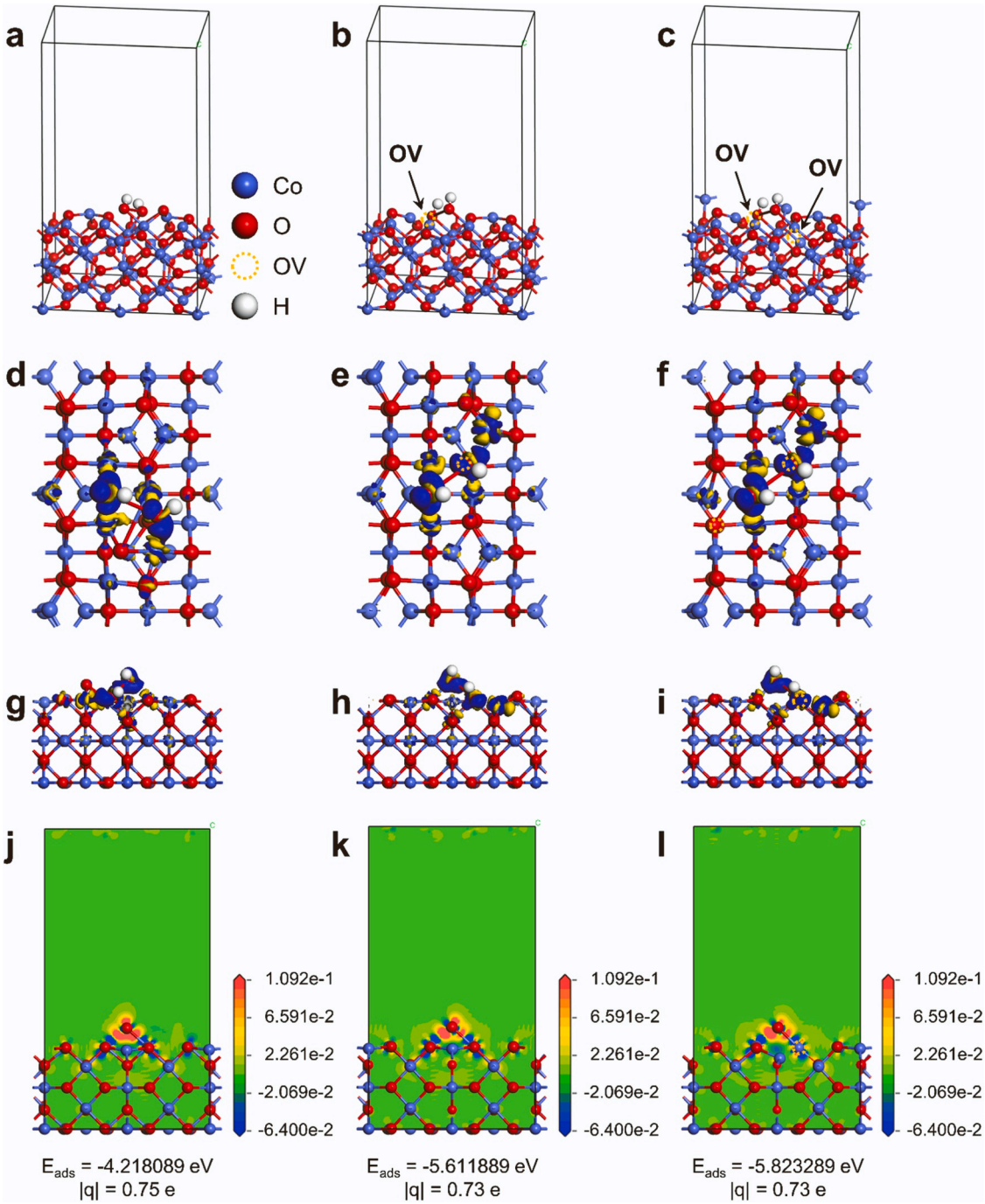

Fig. 10. (a-c) Optimized configuration of H_2O_2 adsorption and (d-l) CDD of H_2O_2 on Co_3O_4 (220) planes (d-f: 3D top views, g-i: 3D side views, and j-l: 2D side views): (a, d, g, j) without OV, (b, e, h, k) with 1 OV, and (c, f, i, l) with 2 OV (isosurface value = 0.03 electrons/Å^3; blue and yellow represent electron density accumulation and depletion, respectively).

caused $^{\bullet}$OH to be consumed over time (Fig. 8 h), leading to enhanced H_2O_2 activation (Fig. 9b). Finally, SDZ was degraded because of electron-withdrawing effect of the metastable YCO-3/H_2O_2 complex, minor role of $^{\bullet}$OH, and significant role of $O_2^{\bullet-}$ (Eqs. 25, 26).

$$H_2O_2 + e_{aq}^- \rightarrow {}^{\cdot}OH + OH^- \left(k = 1.110^{10}\ M^{-1}s^{-1}\right) \quad (24)$$

$$SDZ - e_{aq}^- \rightarrow \text{intermediates} + CO_2 + H_2O \quad (25)$$

$$SDZ + {}^{\cdot}OH/O_2^{\cdot-} \rightarrow \text{intermediates} + CO_2 + H_2O \quad (26)$$

3.8. SDZ degradation pathways

DFT calculations, like ESP and Fukui indices, can be used to investigate how a particular pollutant degrades, which is strongly reliant on its reaction sites. Fukui indices consist of f^-, f^0, and f^+, which are typical for reaction sites with high ability to be attacked by electrophiles ($^1O_2$, metastable YCO-3/H_2O_2 complex), radicals ($^{\bullet}$OH, $O_2^{\bullet-}$), and nucleophiles (OH^-), respectively [85]. In addition, electrophiles tend to attack LUMO, while nucleophiles prefer the sites where HOMO is high. Based on the optimized structure of SDZ in Fig. 12(a), HOMO and LUMO, as illustrated in Fig. 12(b, c), are found to appear mainly at C3, C4, C11, N16 for HOMO and C5, C6, N17, N18 for LUMO. As to ESP (Fig. 12d),

Table 3
Mulliken charges of H and O atoms in H_2O_2 molecule, number of charges transferred to H_2O_2, and O-O bond length of H_2O_2 before and after adsorption on different Co_3O_4 (220) planes:.

Adsorption model	Mulliken charge (e)				Charge transferred q (e)	O-O bond length (Å)
	H1	H2	O1	O2		
H_2O_2	0.54	0.54	-0.54	-0.54	0.00	1.468
Co_3O_4 (220) without OV/ H_2O_2	0.30	0.40	-0.72	-0.73	-0.75	2.842
Co_3O_4 (220) with 1 OV/ H_2O_2	0.39	0.39	-0.73	-0.78	-0.73	2.890
Co_3O_4 (220) with 2 OV/ H_2O_2	0.40	0.39	-0.74	-0.78	-0.73	2.957

areas with positive ESP distributed throughout two rings, making these rings tend to receive attacks mostly. Furthermore, C3, C4, C11, O14, O15, and N16 have high f^-, making these sites vulnerable to electrophiles, according to f^-, f°, and f^+-mapped electron density and Fukui indices in Fig. 12(e-h). Meanwhile, C5, C6, O15, N17, and N18 with high f^+ are easily hydroxylated by OH^- in the solution. Finally, C5, C6, O15, N16, and N17 are the sites most susceptible to radical attacks by $^\bullet OH$ (minor), $O_2^{\bullet-}$ (major) because of their high f°.

Accordingly, the general degradation pathways of SDZ in YCO-3/H_2O_2 system with the participation of several intermediates (Table S14), detected based on experimentally determined *m/z* in Fig. S21 and DFT above, were suggested in Fig. 12(k). Overall, there were eight main possible pathways, including (1) hydroxylation; (2) hydroxylation and -NH_2 oxidation; (3) C-N bond cleavage and -NH_2 oxidation; (4) C-N bond cleavage, -NH_2 oxidation, and H_2 addition; (5) -NH_2 oxidation and H_2 addition; (6) deamination and H_2 addition; (7) deamination and hydroxylation; and (8) H_2 addition. In pathway (1), OH^- addition at C5, C6, N17, and N18 (high f^+) could result in the formation of five probable intermediates (SD14a and SD15a-d in Fig. 12i). Among SD15a-d, SD15a and SD15c were more preferable due to their lower free energy (Fig. 12j, Table S13). Afterwards, a number of reactions involving SD14a, SD15a, and SD15c took place at active sites (Fig. S34, S37, S38) to complete the pathway (1) after transformation into SD6, SD12a, and SD12d (see active sites in Fig. S22, SD29, SD32). In pathway (2), nucleophilic attacks at C5, C6, and electrophilic or radical attacks at N16 led to the formation of SD16a (free energy lower than that of SD16b, Fig. 12j and Table S13) and SD18, which were then transformed into SD9a, SD9b, SD2, SD13, SD9e for SD16a (active sites in Fig. S39, S25, S26, S33) and SD14c, SD11b for SD18 (active sites in Fig. S41, S36) before mineralization by the appearance of CO_2 and H_2O. In pathway (3), SD9a was formed due to the C-N bond cleavage of C5-N17, C6-N18 and the oxidation of -NH_2 at N16. After that, it followed several transformations as SD16a did to finish this pathway (see active sites in Fig. S25, S26, S33). SD9b, on the other hand, initiated the pathway (4) by the addition of H_2 at S20-O15 besides -NH_2 oxidation and C-N bond cleavage as the way through which SD9a appeared in pathway (3). This intermediate was subsequently transformed into SD2 before finishing with the formation of CO_2 and H_2O at the end. Similarly, pathways (5), (6), (7), and (8), which were started by the formation of SD14b, SD8, SD10b&SD17, and SD11a, respectively, continued to proceed to form other small molecules based on active sites (Fig. S23, S24, S27, S28, S30, S31, S35, S40) and were mineralized into CO_2 and H_2O_2.

4. Conclusions

Herein, the appearance of OV was shown to alter the electronic properties of YCO-X. Specific variation was observed for the local electron density, charge density, and delocalization of Co atoms around OV. As the OV increased, the local electron density and delocalization increased, while the charge density decreased, thereby increasing the

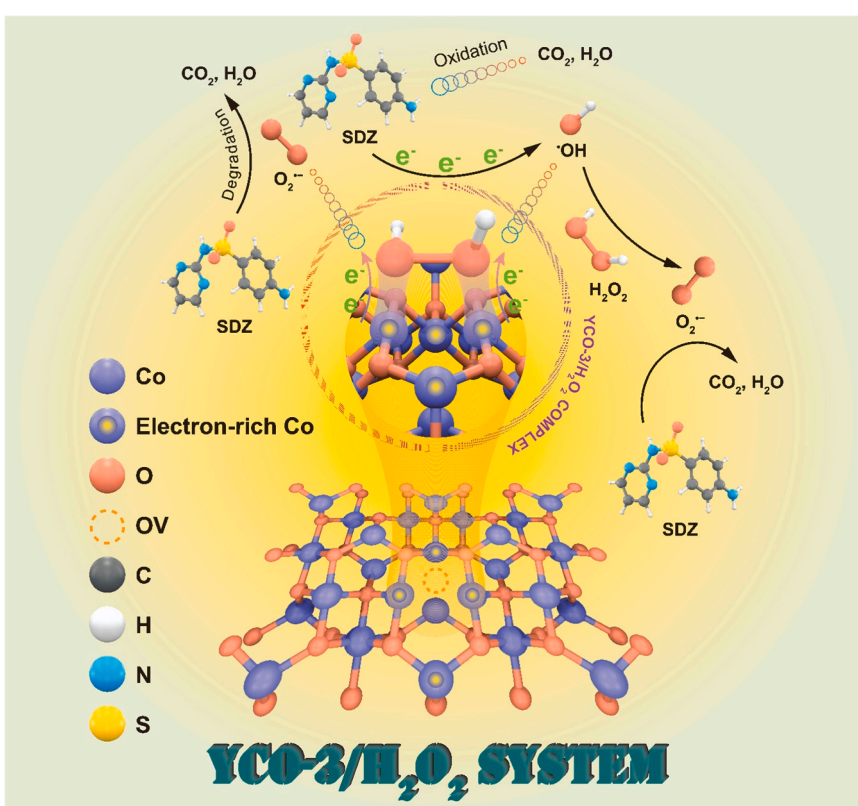

Fig. 11. Schematic illustration of the main mechanism for SDZ degradation in YCO-3/H_2O_2 system.

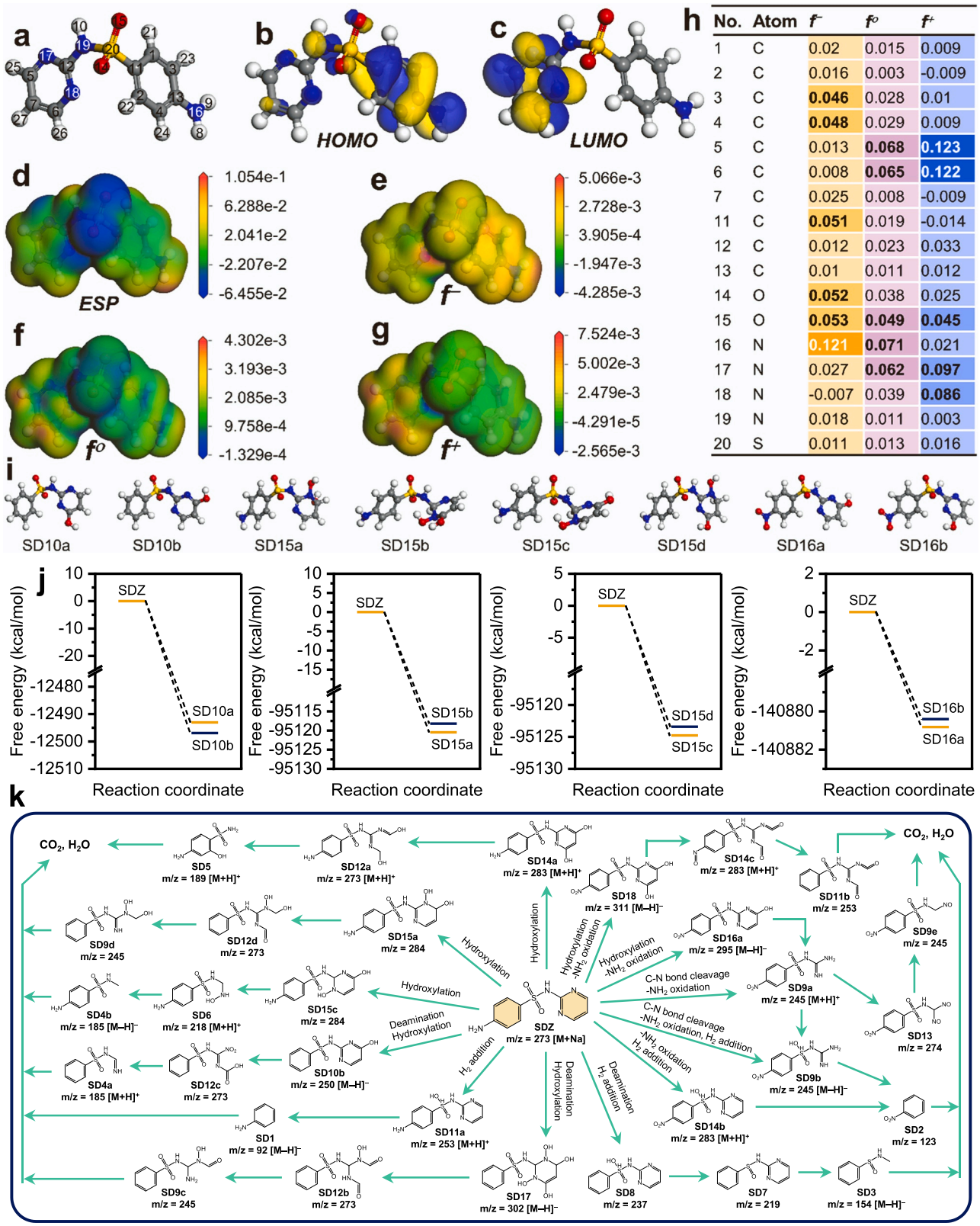

No.	Atom	f^-	f^o	f^+
1	C	0.02	0.015	0.009
2	C	0.016	0.003	-0.009
3	C	**0.046**	0.028	0.01
4	C	**0.048**	0.029	0.009
5	C	0.013	**0.068**	**0.123**
6	C	0.008	**0.065**	**0.122**
7	C	0.025	0.008	-0.009
11	C	**0.051**	0.019	-0.014
12	C	0.012	0.023	0.033
13	C	0.01	0.011	0.012
14	O	**0.052**	0.038	0.025
15	O	**0.053**	**0.049**	**0.045**
16	N	**0.121**	**0.071**	0.021
17	N	0.027	**0.062**	**0.097**
18	N	-0.007	0.039	**0.086**
19	N	0.018	0.011	0.003
20	S	0.011	0.013	0.016

Fig. 12. (a) Optimized structure; (b, c) HOMO, LUMO; (d) ESP; (e-g) electron density mapped by f^-, f^o, f^+ (isosurface value = 0.017 electrons/Å^3); and (h) Fukui indices of SDZ; (i) optimized structures of several possible intermediates and (j) their corresponding free-energy diagrams; (k) degradation pathways of SDZ in YCO-3/H_2O_2 system.

conductivity due to the reduction of the work function and the enhanced electron-donating capacity of Co sites. As a result, the subsequent adsorption of H_2O_2 on the delocalized electron-rich Co sites was enhanced as reflected by the decreased adsorption energy and the prolonged O-O bond in the H_2O_2 molecule. From the experimental results, $^{\bullet}OH$ and $O_2^{\bullet-}$ were recognized as the two main species generated from the activation of H_2O_2, but the decrease of $^{\bullet}OH$ over time a long with its insignificant contribution made it easy for $O_2^{\bullet-}$ to be the main contributor to the degradation of SDZ, and was enhanced in the presence of SDZ as an electron donor through electron transfer. These results explored a pathway that enhanced the generation of $O_2^{\bullet-}$ through electron transfer for antibiotic degradation in Fenton-like process.

CRediT authorship contribution statement

Ta Cong Khiem: Data curation; **Eilhann Kwon**: preparation of figures; **Jechan Lee**: Writing – original draft preparation. **Wen-Da Oh**: Visualization, Investigation. **Xiaoguang Duan**: Visualization, Investigation; **Haitao Wang**: Writing – review & editing. **Nguyen Nhat Huy**: Data curation. **Stanisław Wacławek**: Writing – review & editing. **Grzegorz Lisak**: Investigation. **Farshid Ghanbari**: Writing – original draft preparation. **Kun-Yi Andrew Lin**: Writing – original draft preparation.

Declaration of Competing Interest

The authors declare that they have no known competing financial interests or personal relationships that could have appeared to influence the work reported in this paper.

Data Availability

The authors are unable or have chosen not to specify which data has been used.

Appendix A. Supporting information

Supplementary data associated with this article can be found in the online version at doi:10.1016/j.apcatb.2023.123490.

References

[1] X. Wang, J. Jing, M. Zhou, R. Dewil, Recent advances in H2O2-based advanced oxidation processes for removal of antibiotics from wastewater, Chin. Chem. Lett. 34 (2023), 107621.

[2] Y. Wang, L. Yu, R. Wang, Y. Wang, X. Zhang, Reactivity of carbon spheres templated Ce/LaCo0. 5Cu0. 5O3 in the microwave induced H2O2 catalytic degradation of salicylic acid: characterization, kinetic and mechanism studies, J. Colloid Interface Sci. 574 (2020) 74–86.

[3] N. Geng, W. Chen, H. Xu, M. Ding, Z. Xie, A. Wang, Removal of tetracycline hydrochloride by Z-scheme heterojunction sono-catalyst acting on ultrasound/H2O2 system, Process Saf. Environ. Prot. 165 (2022) 93–101.

[4] C. Liu, H. Dai, C. Tan, Q. Pan, F. Hu, X. Peng, Photo-Fenton degradation of tetracycline over Z-scheme Fe-g-C3N4/Bi2WO6 heterojunctions: mechanism insight, degradation pathways and DFT calculation, Appl. Catal. B: Environ. 310 (2022), 121326.

[5] X. Li, Y. Jia, J. Zhang, Y. Qin, Y. Wu, M. Zhou, J. Sun, Efficient removal of tetracycline by H2O2 activated with iron-doped biochar: Performance, mechanism, and degradation pathways, Chin. Chem. Lett. 33 (2022) 2105–2110.

[6] H. Zeng, G. Zhang, Q. Ji, H. Liu, X. Hua, H. Xia, M. Sillanpää, J. Qu, pH-independent production of hydroxyl radical from atomic H*-mediated electrocatalytic H2O2 reduction: a green Fenton process without byproducts, Environ. Sci. Technol. 54 (2020) 14725–14731.

[7] H. Zhang, C. Zhou, H. Zeng, H. Wu, L. Yang, L. Deng, Z. Shi, ZIF-8 assisted synthesis of magnetic core–shell Fe3O4@ CuS nanoparticles for efficient sulfadiazine degradation via H2O2 activation: Performance and mechanism, J. Colloid Interface Sci. 594 (2021) 502–512.

[8] R.-R. Ding, W.-Q. Li, C.-S. He, Y.-R. Wang, X.-C. Liu, G.-N. Zhou, Y. Mu, Oxygen vacancy on hollow sphere CuFe2O4 as an efficient Fenton-like catalysis for organic pollutant degradation over a wide pH range, Appl. Catal. B: Environ. 291 (2021), 120069.

[9] C. Dong, Z. Qu, X. Jiang, Y. Ren, Tuning oxygen vacancy concentration of MnO2 through metal doping for improved toluene oxidation, J. Hazard. Mater. 391 (2020), 122181.

[10] L. Li, M. Cheng, E. Almatrafi, L. Qin, S. Liu, H. Yi, L. Yang, Z. Chen, D. Ma, M. Zhang, Tuning the intrinsic catalytic sites of magnetite to concurrently enhance the reduction of H2O2 and O2: mechanism analysis and application potential evaluation, J. Hazard. Mater. (2023), 131800.

[11] H. Chen, M. Yang, S. Tao, G. Chen, Oxygen vacancy enhanced catalytic activity of reduced Co3O4 towards p-nitrophenol reduction, Appl. Catal. B: Environ. 209 (2017) 648–656.

[12] L. Liu, Q. Liu, Y. Wang, J. Huang, W. Wang, L. Duan, X. Yang, X. Yu, X. Han, N. Liu, Nonradical activation of peroxydisulfate promoted by oxygen vacancy-laden NiO for catalytic phenol oxidative polymerization, Appl. Catal. B: Environ. 254 (2019) 166–173.

[13] X. Liu, Q. Xia, J. Zhou, B. Li, S. Zhao, L. Chen, A. Khan, X. Li, A. Xu, Morphology-dependent activation of hydrogen peroxide with Cu2O for tetracycline hydrochloride degradation in bicarbonate aqueous solution, J. Environ. Sci. 137 (2024) 567–579.

[14] L. Kong, G. Fang, Z. Fang, Y. Zou, F. Zhu, D. Zhou, J. Zhan, Peroxymonosulfate activation by localized electrons of ZnO oxygen vacancies for contaminant degradation, Chem. Eng. J. 416 (2021), 128996.

[15] Y. Li, T. Chen, S. Zhao, P. Wu, Y. Chong, A. Li, Y. Zhao, G. Chen, X. Jin, Y. Qiu, Engineering cobalt oxide with coexisting cobalt defects and oxygen vacancies for enhanced catalytic oxidation of toluene, ACS Catal. 12 (2022) 4906–4917.

[16] X. Yang, C. Lai, L. Li, M. Cheng, S. Liu, H. Yi, M. Zhang, Y. Fu, F. Xu, H. Yan, Oxygen vacancy assisted Mn-CuO Fenton-like oxidation of ciprofloxacin: performance, effects of pH and mechanism, Sep. Purif. Technol. 287 (2022), 120517.

[17] M. Zhu, J. Miao, D. Guan, Y. Zhong, R. Ran, S. Wang, W. Zhou, Z. Shao, Efficient wastewater remediation enabled by self-assembled perovskite oxide heterostructures with multiple reaction pathways, ACS Sustain. Chem. Eng. 8 (2020) 6033–6042.

[18] D. Liu, X. Xue, X. Zhang, Y. Huang, P. Feng, Highly efficient peroxymonosulfate activation by MOFs-derived oxygen vacancy-rich Co3O4/ZnO pn heterojunction nanocomposites to degrade pefloxacin, Sep. Purif. Technol. 305 (2023), 122451.

[19] M. Asnavandi, Y. Yin, Y. Li, C. Sun, C. Zhao, Promoting oxygen evolution reactions through introduction of oxygen vacancies to benchmark NiFe–OOH catalysts, ACS Energy Lett. 3 (2018) 1515–1520.

[20] P. Gao, X. Chen, M. Hao, F. Xiao, S. Yang, Oxygen vacancy enhancing the Fe2O3-CeO2 catalysts in Fenton-like reaction for the sulfamerazine degradation under O2 atmosphere, Chemosphere 228 (2019) 521–527.

[21] X.X. Guo, T.T. Hu, B. Meng, Y. Sun, Y.-F. Han, Catalytic degradation of anthraquinones-containing H2O2 production effluent over layered Co-Cu hydroxides: defects facilitating hydroxyl radicals generation, Appl. Catal. B: Environ. 260 (2020), 118157.

[22] G. Wang, L. Ge, Z. Liu, X. Zhu, S. Yang, K. Wu, P. Jin, X. Zeng, X. Zhang, Activation of peroxydisulfate by defect-rich CuO nanoparticles supported on layered MgO for organic pollutants degradation: An electron transfer mechanism, Chem. Eng. J. 431 (2022), 134026.

[23] H. Li, J. Shang, Z. Yang, W. Shen, Z. Ai, L. Zhang, Oxygen vacancy associated surface Fenton chemistry: surface structure dependent hydroxyl radicals generation and substrate dependent reactivity, Environ. Sci. Technol. 51 (2017) 5685–5694.

[24] J. Qin, Z. Liu, D. Wu, J. Yang, Optimizing the electronic structure of cobalt via synergized oxygen vacancy and Co-NC to boost reversible oxygen electrocatalysis for rechargeable Zn-air batteries, Appl. Catal. B: Environ. 278 (2020), 119300.

[25] K. Zhu, F. Shi, X. Zhu, W. Yang, The roles of oxygen vacancies in electrocatalytic oxygen evolution reaction, Nano Energy 73 (2020), 104761.

[26] X. Ren, M. Gao, Y. Zhang, Z. Zhang, X. Cao, B. Wang, X. Wang, Photocatalytic reduction of CO_2 on BiOX: Effect of halogen element type and surface oxygen vacancy mediated mechanism, Appl. Catal. B: Environ. 274 (2020), 119063.

[27] Z. Li, W. Yang, L. Xie, Y. Li, Y. Liu, Y. Sun, Y. Bu, X. Mi, S. Zhan, W. Hu, Prominent role of oxygen vacancy for superoxide radical and hydroxyl radical formation to promote electro-Fenton like reaction by W-doped CeO2 composites, Appl. Surf. Sci. 549 (2021), 149262.

[28] K. Pan, C. Yang, J. Hu, W. Yang, B. Liu, J. Yang, S. Liang, K. Xiao, H. Hou, Oxygen vacancy mediated surface charge redistribution of Cu-substituted LaFeO3 for degradation of bisphenol A by efficient decomposition of H2O2, J. Hazard. Mater. 389 (2020), 122072.

[29] D. Mao, S. Yang, Y. Hu, H. He, S. Yang, S. Zheng, C. Sun, Z. Jiang, X. Qu, P. K. Wong, Efficient CO_2 photoreduction triggered by oxygen vacancies in ultrafine Bi5O7Br nanowires, Appl. Catal. B: Environ. 321 (2023), 122031.

[30] N. Zhang, J. Chen, Z. Fang, E.P. Tsang, Ceria accelerated nanoscale zerovalent iron assisted heterogenous Fenton oxidation of tetracycline, Chem. Eng. J. 369 (2019) 588–599.

[31] L. Xie, X. Liu, J. Chang, C. Zhang, Y. Li, H. Zhang, S. Zhan, W. Hu, Enhanced redox activity and oxygen vacancies of perovskite triggered by copper incorporation for the improvement of electro-Fenton activity, Chem. Eng. J. 428 (2022), 131352.

[32] J. Li, W. Ma, D. Zhong, K. Li, J. Ma, S. Zhang, X. Du, Oxygen vacancy concentration modulation of perovskite-based heterogeneous catalysts for Fenton-like oxidation of tetracycline, J. Clean. Prod. 362 (2022), 132469.

[33] J. Zan, H. Song, S. Zuo, X. Chen, D. Xia, D. Li, M.I.L.-53 (Fe)-derived, Fe2O3 with oxygen vacancy as Fenton-like photocatalysts for the elimination of toxic organics in wastewater, J. Clean. Prod. 246 (2020), 118971.

[34] C. Lai, L. Yang, L. Li, D. Ma, M. Cheng, S. Liu, M. Zhang, H. Yan, C. Tang, Z. Chen, Design of a highly efficient Cu-based catalyst with two functional areas: The role of

Cu0 and oxygen vacancies in Fenton-like system, Chem. Eng. J. 464 (2023), 142420.
[35] K. Hou, Z. Pi, F. Chen, L. He, F. Yao, S. Chen, X. Li, H. Dong, Q. Yang, Trace-dissolved S (-II) triggers the Fe (III)-activated H2O2 process for organic pollutant degradation by promoting the Fe (III)/Fe (II) Cycle: kinetics, toxicity, and mechanisms, ACS EST Eng. 2 (2022) 2174–2186.
[36] A. Gu, K. Chen, X. Zhou, C. Gong, P. Wang, Y. Jiao, P. Mao, K. Chen, J. Lu, Y. Yang, Trimetallic MOFs-derived Fe-Co-Cu oxycarbide toward peroxymonosulfate activation for efficient trichlorophenol degradation via high-valent metal-oxo species, Chem. Eng. J. 468 (2023), 143444.
[37] T.C. Khiem, N.N. Huy, E. Kwon, S. Wacławek, A. Ebrahimi, W.-D. Oh, S. Ghotekar, Y.F. Tsang, W.-H. Chen, K.-Y.A. Lin, Tailoring oxygen vacancies in Co3O4 yolk-shell nanospheres via for boosted peroxymonosulfate activation: Single-electron transfer and high-valent Co-oxo species-dominated non-radical pathways, Chem. Eng. J. (2023), 146404.
[38] T.C. Khiem, N.N. Huy, E. Kwon, X. Duan, S. Wacławek, J. Bedia, Y.-C. Tsai, A. Ebrahimi, F. Ghanbari, K.-Y.A. Lin, Hetero-Interface-Engineered Sulfur Vacancy and Oxygen Doping in Hollow Co9S8/Fe7S8 Nanospheres towards Monopersulfate Activation for Boosting Intrinsic Electron Transfer in Paracetamol Degradation, Appl. Catal. B: Environ. (2023), 122550.
[39] C. Wang, X. Wang, H. Wang, L. Zhang, Y. Wang, C.-L. Dong, Y.-C. Huang, P. Guo, R. Cai, S.J. Haigh, Low-coordinated Co-N3 sites induce peroxymonosulfate activation for norfloxacin degradation via high-valent cobalt-oxo species and electron transfer, J. Hazard. Mater. 455 (2023), 131622.
[40] Z. Song, B. Wang, J. Yu, C. Ma, C. Zhou, T. Chen, Q. Yan, K. Wang, L. Sun, Density functional study on the heterogeneous oxidation of NO over α-Fe2O3 catalyst by H2O2: effect of oxygen vacancy, Appl. Surf. Sci. 413 (2017) 292–301.
[41] W. Qu, C. Chen, Z. Tang, D. Xia, D. Ma, Y. Huang, Q. Lian, C. He, D. Shu, B. Han, Electron-rich/poor reaction sites enable ultrafast confining Fenton-like processes in facet-engineered BiOI membranes for water purification, Appl. Catal. B: Environ. 304 (2022), 120970.
[42] S. Jiang, G. Su, J. Wu, C. Song, Z. Lu, C. Wu, Y. Wang, P. Wang, M. He, Y. Zhao, Co3O4/CoFe2O4 hollow nanocube multifunctional nanozyme with oxygen vacancies for deep-learning-assisted smartphone biosensing and organic pollutant degradation, ACS Appl. Mater. Interfaces 15 (2023) 11787–11801.
[43] T. Li, Y. Zou, Z. Liu, Magnetic-thermal external field activate the pyro-magnetic effect of pyroelectric crystal (NaNbO3) to build a promising multi-field coupling-assisted photoelectrochemical water splitting system, Appl. Catal. B: Environ. 328 (2023), 122486.
[44] N.V. Klassen, D. Marchington, H.C. McGowan, H2O2 determination by the I3-method and by KMnO4 titration, Anal. Chem. 66 (1994) 2921–2925.
[45] C. Chen, G. Qiu, T. Wang, Z. Zheng, M. Huang, B. Li, Modulating oxygen vacancies on bismuth-molybdate hierarchical hollow microspheres for photocatalytic selective alcohol oxidation with hydrogen peroxide production, J. Colloid Interface Sci. 592 (2021) 1–12.
[46] S. Zhao, X. Zhao, Insights into the role of singlet oxygen in the photocatalytic hydrogen peroxide production over polyoxometalates-derived metal oxides incorporated into graphitic carbon nitride framework, Appl. Catal. B: Environ. 250 (2019) 408–418.
[47] Y. Zheng, K. Fu, Z. Yu, Y. Su, R. Han, Q. Liu, Oxygen vacancies in a catalyst for VOCs oxidation: synthesis, characterization, and catalytic effects, J. Mater. Chem. A 10 (2022) 14171–14186.
[48] Z. Liang, C. Zhang, Y. Xu, W. Zhang, H. Zheng, R. Cao, Dual tuning of ultrathin α-Co (OH) 2 nanosheets by solvent engineering and coordination competition for efficient oxygen evolution, ACS Sustain. Chem. Eng. 7 (2018) 3527–3535.
[49] G. Chai, W. Zhang, L.F. Liotta, M. Li, Y. Guo, A. Giroir-Fendler, Total oxidation of propane over Co3O4-based catalysts: Elucidating the influence of Zr dopant, Appl. Catal. B: Environ. 298 (2021), 120606.
[50] Y. Jian, M. Tian, C. He, J. Xiong, Z. Jiang, H. Jin, L. Zheng, R. Albilali, J.-W. Shi, Efficient propane low-temperature destruction by Co3O4 crystal facets engineering: Unveiling the decisive role of lattice and oxygen defects and surface acid-base pairs, Appl. Catal. B: Environ. 283 (2021), 119657.
[51] Q. Zhang, S. Mo, B. Chen, W. Zhang, C. Huang, D. Ye, Hierarchical Co3O4 nanostructures in-situ grown on 3D nickel foam towards toluene oxidation, Mol. Catal. 454 (2018) 12–20.
[52] R. Zhang, Y.-C. Zhang, L. Pan, G.-Q. Shen, N. Mahmood, Y.-H. Ma, Y. Shi, W. Jia, L. Wang, X. Zhang, Engineering cobalt defects in cobalt oxide for highly efficient electrocatalytic oxygen evolution, Acs Catal. 8 (2018) 3803–3811.
[53] Y.C. Zhang, N. Afzal, L. Pan, X. Zhang, J.J. Zou, Structure-activity relationship of defective metal-based photocatalysts for water splitting: experimental and theoretical perspectives, Adv. Sci. 6 (2019) 1900053.
[54] Q. Ma, F. Cui, J. Zhang, X. Qi, T. Cui, Surface engineering of Co3O4 nanoribbons forming abundant oxygen-vacancy for advanced supercapacitor, Appl. Surf. Sci. 578 (2022), 152001.
[55] X. Wang, X. Li, J. Mu, S. Fan, X. Chen, L. Wang, Z. Yin, M. Tade, S. Liu, Oxygen Vacancy-rich Porous Co3O4 Nanosheets toward Boosted NO Reduction by CO and CO Oxidation: Insights into the Structure–Activity Relationship and Performance Enhancement Mechanism, ACS Appl. Mater. Interfaces 11 (2019) 41988–41999.
[56] Z. Ren, Z. Wu, W. Song, W. Xiao, Y. Guo, J. Ding, S.L. Suib, P.-X. Gao, Low temperature propane oxidation over Co3O4 based nano-array catalysts: Ni dopant effect, reaction mechanism and structural stability, Appl. Catal. B: Environ. 180 (2016) 150–160.
[57] Y. Rao, Y. Zhang, F. Han, H. Guo, Y. Huang, R. Li, F. Qi, J. Ma, Heterogeneous activation of peroxymonosulfate by LaFeO3 for diclofenac degradation: DFT-assisted mechanistic study and degradation pathways, Chem. Eng. J. 352 (2018) 601–611.
[58] X. Wei, K. Li, X. Zhang, Q. Tong, J. Ji, Y. Cai, B. Gao, W. Zou, L. Dong, CeO2 nanosheets with anion-induced oxygen vacancies for promoting photocatalytic toluene mineralization: Toluene adsorption and reactive oxygen species, Appl. Catal. B: Environ. 317 (2022), 121694.
[59] L. Chen, T. Li, J. Zhang, J. Wang, P. Chen, M. Fu, J. Wu, D. Ye, Chemisorbed superoxide species enhanced the high catalytic performance of Ag/Co3O4 nanocubes for soot oxidation, ACS Appl. Mater. Interfaces 13 (2021) 21436–21449.
[60] Z. Xiao, Y.-C. Huang, C.-L. Dong, C. Xie, Z. Liu, S. Du, W. Chen, D. Yan, L. Tao, Z. Shu, Operando identification of the dynamic behavior of oxygen vacancy-rich Co3O4 for oxygen evolution reaction, J. Am. Chem. Soc. 142 (2020) 12087–12095.
[61] T.C. Khiem, X. Duan, W.-J. Liu, Y.-K. Park, H.M. Bui, W.-D. Oh, S. Ghotekar, Y. F. Tsang, K.-Y.A. Lin, MOF-templated hollow cobalt sulfide as an enhanced oxone activator for degradation of UV absorber: key role of sulfur vacancy-induced highly active coii sites, Chem. Eng. J. (2022), 139699.
[62] J. Hu, Y. Li, Y. Zou, L. Lin, B. Li, X.-y Li, Transition metal single-atom embedded on N-doped carbon as a catalyst for peroxymonosulfate activation: a DFT study, Chem. Eng. J. 437 (2022), 135428.
[63] L. Sun, Y. Feng, K. Ma, X. Jiang, Z. Gao, J. Wang, N. Jiang, X. Liu, Synergistic effect of single-atom Ag and hierarchical tremella-like g-C3N4: electronic structure regulation and multi-channel carriers transport for boosting photocatalytic performance, Appl. Catal. B: Environ. 306 (2022), 121106.
[64] S. Anantharaj, H. Sugime, S. Noda, Surface amorphized nickel hydroxy sulphide for efficient hydrogen evolution reaction in alkaline medium, Chem. Eng. J. 408 (2021), 127275.
[65] Z. Wang, W. Liu, J. Bao, Y. Song, X. She, Y. Hua, G. Lv, J. Yuan, H. Li, H. Xu, Modulating electronic structure of ternary NiMoV LDH nanosheet array induced by doping engineering to promote urea oxidation reaction, Chem. Eng. J. 430 (2022), 133100.
[66] J. Weinstein, B.H. Bielski, Kinetics of the interaction of perhydroxyl and superoxide radicals with hydrogen peroxide. The Haber-Weiss reaction, J. Am. Chem. Soc. 101 (1979) 58–62.
[67] Y. Bao, W. Liu, J. Cao, J. Zhang, M. Xing, Self-Neutralized Conditions Constructed by Amphoteric Zinc in Cobalt-Induced Peroxymonosulfate Activation for Sustainable Degradation of Organic Pollutants, ACS ES&T Engineering, (2023).
[68] M. Ran, H. Xu, Y. Bao, Y. Zhang, J. Zhang, M. Xing, Selective production of CO from organic pollutants by coupling piezocatalysis and advanced oxidation processes, Angew. Chem. 135 (2023), e202303728.
[69] E.-T. Yun, J.H. Lee, J. Kim, H.-D. Park, J. Lee, Identifying the nonradical mechanism in the peroxymonosulfate activation process: singlet oxygenation versus mediated electron transfer, Environ. Sci. Technol. 52 (2018) 7032–7042.
[70] X. Liu, X. Yan, W. Liu, Q. Yan, M. Xing, Switching of radical and nonradical pathways through the surface defects of Fe3O4/MoOxSy in a Fenton-like reaction, Sci. Bull. 68 (2023) 603–612.
[71] Y. He, J. Qian, P. Wang, J. Wu, B. Lu, S. Tang, P. Gao, Acceleration of levofloxacin degradation by combination of multiple free radicals via MoS2 anchored in manganese ferrite doped perovskite activated PMS under visible light, Chem. Eng. J. 431 (2022), 133933.
[72] P. Liang, C. Zhang, X. Duan, H. Sun, S. Liu, M.O. Tade, S. Wang, N-doped graphene from metal–organic frameworks for catalytic oxidation of p-hydroxylbenzoic acid: N-functionality and mechanism, ACS Sustain. Chem. Eng. 5 (2017) 2693–2701.
[73] J. Guo, H. Jia, A. Zhang, Z. Pei, M. Luo, J. Xue, Q. Shen, X. Liu, B. Xu, MIL-100 (Fe) with mix-valence coordinatively unsaturated metal site as Fenton-like catalyst for efficiently removing tetracycline hydrochloride: Boosting Fe (III)/Fe (II) cycle by photoreduction, Sep. Purif. Technol. 262 (2021), 118334.
[74] X. Chen, W. Fu, Z. Yang, Y. Yang, Y. Li, H. Huang, X. Zhang, B. Pan, Enhanced H2O2 utilization efficiency in Fenton-like system for degradation of emerging contaminants: Oxygen vacancy-mediated activation of O2, Water Res. 230 (2023), 119562.
[75] X. Zhou, Q. Zhao, J. Wang, Z. Chen, Z. Chen, Nonradical oxidation processes in PMS-based heterogeneous catalytic system: Generation, identification, oxidation characteristics, challenges response and application prospects, Chem. Eng. J. 410 (2021), 128312.
[76] H.V. Molamahmood, W. Geng, Y. Wei, J. Miao, S. Yu, A. Shahi, C. Chen, M. Long, Catalyzed H2O2 decomposition over iron oxides and oxyhydroxides: Insights from oxygen production and organic degradation, Chemosphere 291 (2022), 133037.
[77] M.M. Tarpey, I. Fridovich, Methods of detection of vascular reactive species: nitric oxide, superoxide, hydrogen peroxide, and peroxynitrite, Circ. Res. 89 (2001) 224–236.
[78] T.C. Khiem, D.D. Tuan, E. Kwon, N.N. Huy, W.-D. Oh, W.-H. Chen, K.-Y.A. Lin, Degradation of dihydroxybenzophenone through monopersulfate activation over nanostructured cobalt ferrites with various morphologies: A comparative study, Chem. Eng. J. 450 (2022), 137798.
[79] Q. Wang, C. Liu, D. Zhou, X. Chen, M. Zhang, K. Lin, Degradation of bisphenol a using peroxymonosulfate activated by single-atomic cobalt catalysts: Different reactive species at acidic and alkaline pH, Chem. Eng. J. 439 (2022), 135002.
[80] Y. Zong, X. Guan, J. Xu, Y. Feng, Y. Mao, L. Xu, H. Chu, D. Wu, Unraveling the overlooked involvement of high-valent cobalt-oxo species generated from the cobalt (II)-activated peroxymonosulfate process, Environ. Sci. Technol. 54 (2020) 16231–16239.
[81] W. Zhong, Q. Peng, K. Liu, X. Tang, Y. Zhang, J. Xing, Building Cu0/CuFe2O4 framework to efficiently degrade tetracycline and improve utilization of H2O2 in Fenton-like system, Chem. Eng. J. 474 (2023), 145522.
[82] C. Du, S. Yang, D. Ding, T. Cai, R. Chen, Origin of synergistic effect between Fe/Mn minerals and biochar for peroxymonosulfate activation, Chem. Eng. J. 453 (2023), 139899.

[83] J. Tan, X. Chen, M. Shang, J. Cui, D. Li, F. Yang, Z. Zhang, H. Zhang, Q. Wu, Y. Li, N-doped biochar mediated peroxydisulfate activation for selective degradation of bisphenol A: the key role of potential difference-driven electron transfer mechanism, Chem. Eng. J. 468 (2023), 143476.

[84] C. Wang, F. Chen, C. Hu, T. Ma, Y. Zhang, H. Huang, Efficient piezocatalytic H2O2 production of atomic-level thickness Bi4Ti3O12 nanosheets with surface oxygen vacancy, Chem. Eng. J. 431 (2022), 133930.

[85] X.-Y. Jiang, Y.-K. Park, J.-C. Wen, H.M. Bui, Y.-F. Lin, S. Sirivithayapakorn, T. C. Khiem, V.S. Munagapati, K.-Y.A. Lin, Hollow-architected Co3O4 for enhancing Oxone activation to eliminate an anesthetic, benzocaine, from water: a structure-property investigation with degradation pathway and eco-toxicity, J. Taiwan Inst. Chem. Eng. 150 (2023), 105042.